

Deep *Chandra* observations of Pictor A

M.J. Hardcastle^{1*}, E. Lenc^{2,3}, M. Birkinshaw⁴, J.H. Croston^{5,6}, J.L. Goodger^{1†},
H.L. Marshall⁷, E.S. Perlman⁸, A. Siemiginowska⁹, Ł. Stawarz¹⁰ and D.M. Worrall⁴

¹ School of Physics, Astronomy and Mathematics, University of Hertfordshire, College Lane, Hatfield AL10 9AB, UK

² Sydney Institute for Astronomy, School of Physics, The University of Sydney, NSW 2006, Australia

³ ARC Centre of Excellence for All-Sky Astrophysics (CAASTRO), Redfern, NSW 2016, Australia

⁴ H.H. Wills Physics Laboratory, University of Bristol, Tyndall Avenue, Bristol BS8 1TL, UK

⁵ School of Physics and Astronomy, University of Southampton, Southampton SO17 1BJ, UK

⁶ Institute of Continuing Education, University of Cambridge, Madingley Hall, Madingley, CB23 8AQ, UK

⁷ Kavli Institute for Astrophysics and Space Research, Massachusetts Institute of Technology, 77 Massachusetts Ave., Cambridge, MA 02139, USA

⁸ Department of Physics and Space Sciences, Florida Institute of Technology, 150 W. University Blvd., Melbourne, FL 32901, USA

⁹ Harvard-Smithsonian Center for Astrophysics, 60 Garden Street, Cambridge, MA 02138, USA

¹⁰ Astronomical Observatory, Jagiellonian University, ul. Orla 171, 30-244 Kraków, Poland

10 September 2018

ABSTRACT

We report on deep *Chandra* observations of the nearby broad-line radio galaxy Pictor A, which we combine with new Australia Telescope Compact Array (ATCA) observations. The new X-ray data have a factor 4 more exposure than observations previously presented and span a 15-year time baseline, allowing a detailed study of the spatial, temporal and spectral properties of the AGN, jet, hotspot and lobes. We present evidence for further time variation of the jet, though the flare that we reported in previous work remains the most significantly detected time-varying feature. We also confirm previous tentative evidence for a faint counterjet. Based on the radio through X-ray spectrum of the jet and its detailed spatial structure, and on the properties of the counterjet, we argue that inverse-Compton models can be conclusively rejected, and propose that the X-ray emission from the jet is synchrotron emission from particles accelerated in the boundary layer of a relativistic jet. For the first time, we find evidence that the bright western hotspot is also time-varying in X-rays, and we connect this to the small-scale structure in the hotspot seen in high-resolution radio observations. The new data allow us to confirm that the spectrum of the lobes is in good agreement with the predictions of an inverse-Compton model and we show that the data favour models in which the filaments seen in the radio images are predominantly the result of spatial variation of magnetic fields in the presence of a relatively uniform electron distribution.

Key words: galaxies: jets – galaxies: individual (Pictor A) – X-rays: galaxies

1 INTRODUCTION

1.1 X-ray jets

One of the most important and unexpected discoveries of *Chandra* has been the detection of X-ray emission from the jets of a wide range of different types of radio-loud AGN (see Harris & Krawczynski 2006 and Worrall 2009 for reviews). In Fanaroff & Riley (1974) class I (FRI) radio galaxies, including nearby objects like Cen A (e.g. Hardcastle et al. 2007b) or M87 (e.g. Harris et al. 2003) the jet X-ray emission is believed to be due to the synchrotron mechanism. In this case the X-rays trace electrons with

TeV energies and radiative loss lifetimes of years, and so can give us crucial insights into the location and the nature of particle acceleration in these sources. Dynamical modelling of FRI jets suggests that the particle acceleration regions are associated with bulk deceleration as the jets slow from relativistic to mildly relativistic speeds (e.g. Laing & Bridle 2002). It is possible, in some jets, that a significant fraction of the particle acceleration giving rise to X-ray emission is the result of shocks in the jet related to its interaction with the stellar winds of its internal stars (Wykes et al. 2015). In more powerful FRI jets, like that of M87, this process is probably not energetically capable of producing all the X-ray emission, and instead internal shocks due to jet variability (e.g., Rees 1978) or jet instabilities driving shocks and turbulence (Bicknell & Begelman 1996; Nakamura & Meier 2014), still associated with bulk deceleration, may be required.

* E-mail: m.j.hardcastle@herts.ac.uk

† Present address: Information Services, City University London, Northampton Square, London EC1V 0HB, UK

Our understanding of the X-ray emission from the jets of more powerful radio AGN, including ‘classical double’ FR II radio galaxies and quasars, is much more limited. A wide variety of X-ray counterparts to jets have been seen, ranging from weak X-ray emission from localized ‘jet knots’ in radio galaxies like 3C 403 (Kraft et al. 2005) or 3C 353 (Kataoka et al. 2008) to bright, continuous structures extending over hundreds of kpc in projection, as seen in the prototype of the class, PKS 0637–752 (Schwartz et al. 2000). Two mechanisms have been invoked to explain the X-ray emission from powerful jets. The first is inverse-Compton scattering of the CMB (hereafter IC/CMB) by a population of low-energy electrons (Tavecchio et al. 2000; Celotti et al. 2001). This model relies on high bulk Lorentz factors $\Gamma \gtrsim 10$ and small angles to the line of sight in order to produce detectable X-rays; it has been applied successfully to the bright, continuous X-ray jets in many core-dominated quasars, but has a number of problems in explaining all the observations, particularly the broad-band SED and the spatial variation of the radio/X-ray ratio (Hardcastle 2006), the observed knotty jet X-ray morphology (Tavecchio et al. 2003; Stawarz et al. 2004), the non-detection of the gamma rays predicted in the model (Georganopoulos et al. 2006; Meyer & Georganopoulos 2014; Meyer et al. 2015), and the high degree of observed optical/ultra-violet polarization (Cara et al. 2013). The second process is synchrotron emission, which does not depend on large jet Doppler factors but does require *in situ* particle acceleration as in the FRIs. This model is more often applied to weak X-ray ‘knots’ seen in jets (and counterjets) of radio galaxies, and at present has the weakness that it cannot explain *why* there is localized particle acceleration at certain points in the jets, since, unlike the case of the FRIs, there appears to be no preferred location for X-ray emission, and certainly no association with jet deceleration. (Indeed, there is no direct evidence for significant jet bulk deceleration in FR II jets at all, with the exception of the possible and debatable evidence provided by the X-rays themselves (Hardcastle 2006), and on theoretical grounds the interpretation of the hotspots as jet termination shocks implies supersonic bulk jet motion with respect to the internal jet sound speed.) Detailed studies of individual objects are required to determine how and where the two X-ray emission processes are operating.

The X-ray jet of the FR II radio galaxy Pictor A (Wilson, Young & Shopbell 2001, hereafter W01) provides a vital link between the two extreme classes of source discussed above. Like those of the powerful core-dominated quasars, Pic A’s jet extends for over 100 kpc in projection, and is visible all the way from the core to the terminal hotspot. However, as the source is a lobe-dominated broad-line radio galaxy, its brighter jet is expected to be aligned towards us ($\theta \lesssim 45^\circ$) but *not* to be within a few degrees of the line of sight; *a priori* we would not expect significant IC/CMB X-rays. (A small jet angle to the line of sight would imply a very large, Mpc or larger, physical size for the source.) In addition, the existing *Chandra* data show that the bright region of the jet has a steep spectrum (Hardcastle & Croston 2005, hereafter HC05) and there is a faint but clear X-ray counterjet, neither of which would be expected in IC/CMB models. If the X-rays in Pic A are indeed synchrotron in origin, then it provides us with an opportunity to investigate how a powerful FR II source can accelerate particles along the entire length of its jet. Pic A is also a key object because of its proximity; at $z = 0.035$ it is one of the closest FR IIs, and the closest example of a continuous, 100-kpc-scale X-ray jet. Thus we can investigate the fine structure in the jet, key to tests of *all* possible models of the X-ray emission, at a level not possible in any other powerful object.

Pic A was observed twice in the early part of the *Chandra* mission. A 26-ks observation taken in 2000 provided the first detection of the X-ray jet (W01). In 2002 a 96-ks observation of the X-ray bright W hotspot was taken: these data were used by HC05 in their study of the lobes (see below). In 2009, we re-analysed these data in preparation for a study of the jet and found clear evidence at around the 3σ level for *variability* in discrete regions of the jet between these two epochs: we obtained a new observation which strengthened the evidence for variability in the brightest feature, 34 (projected) kpc from the core, to the 3.4σ level after accounting for trials (Marshall et al. 2010, hereafter M10). Another feature at 49 kpc from the core was found to be variable at the $\sim 3\sigma$ level. The discovery of X-ray variability in the jet of Pic A, the first time it had been seen in an FR II jet, was a remarkable and completely unexpected result which has very significant implications for our understanding of particle acceleration in FR II jets in general. It requires that a significant component of the X-ray emission (and thus the particle acceleration, in a synchrotron model) comes from very small, pc-scale, features embedded in the broader jet. Variability is in principle expected in synchrotron models of X-ray jets, since the synchrotron loss timescales are often very short, implying short lifetimes for discrete features in ‘impulsive’ particle acceleration models. However, the nearby X-ray synchrotron jets in the FRIs Cen A and M87 have been extensively monitored, and most features show little or no evidence for *strong* variability (e.g. Goodger et al. 2010), suggesting that particle acceleration in these jets is generally long-lasting on timescales much longer than the loss timescale. A dramatic exception is the HST-1 knot in the inner jet of M87, which *Chandra* has observed to increase in brightness by a factor ~ 50 on a timescale of years (Harris et al. 2006, 2009). HST-1 in M87 may provide the closest known analogue of what we appear to be seeing in Pic A, but the flares in Pic A are both much more luminous and much further from the AGN. Again, there is no reason to suppose that Pic A is unique among FR II radio galaxies, but, as the closest and brightest of FR II X-ray jets, it provides our best chance of understanding the phenomenon, and it may also provide insight into the presumably related variability on kpc spatial scales that is starting to be seen in gamma rays from lensed blazars (Barnacka et al. 2015).

1.2 Hotspots and lobes

Pic A’s proximity, radio power, and lack of a rich environment emitting thermal X-rays make it a uniquely interesting target in X-rays in several other ways. With the possible exception of Cygnus A (Hardcastle & Croston 2010), where thermal emission from the host cluster is dominant and inverse-Compton emission is hard to detect reliably in the X-ray, it is the brightest lobe inverse-Compton source in the sky: for FR IIs lobe inverse-Compton flux scales roughly with low-frequency radio flux, so this is a direct result of its status as the second brightest FR II radio galaxy in the sky at low frequencies (Robertson 1973). Because of this, the inverse-Compton lobes have been extensively studied in earlier work (W01; Grandi et al. 2003; HC05; Migliori et al. 2007). It also hosts the brightest X-ray hotspot known (e.g., W01; Hardcastle et al. 2004; Tingay et al. 2008). Thus a deep *Chandra* observation of the whole source allows us to study the spatially resolved X-ray spectrum of the lobes and hotspot to a depth not possible in any other FR II. Key questions here are what the spectra of the lobes and hotspot actually are – relatively few sources even provide enough counts to estimate a photon index – and how well they agree with the predictions from the inverse-Compton and synchrotron models for the

Table 1. Details of the *Chandra* observations of Pictor A. The 13 observations used in the paper are listed together with their observation date, duration, pointing position, satellite roll angle and epoch number (observations with the same epoch number are combined when variability is considered).

Obs. ID	Date	Exposure (ks)	Pointing	Satellite roll (deg)	Epoch
346	2000-01-18	25.8	Core	322.4	1
3090	2002-09-17	46.4	W hotspot	88.1	2
4369	2002-09-22	49.1	W hotspot	88.1	2
12039	2009-12-07	23.7	Jet	3.2	3
12040	2009-12-09	17.3	Jet	3.2	3
11586	2009-12-12	14.3	Jet	3.2	3
14357	2012-06-17	49.3	Jet	174.3	4
14221	2012-11-06	37.5	Jet	36.2	5
15580	2012-11-08	10.5	Jet	36.2	5
15593	2013-08-23	49.3	Jet	110.5	6
14222	2014-01-17	45.4	Jet	322.6	7
14223	2014-04-21	50.1	Jet	232.7	8
16478	2015-01-09	26.8	Jet	315.2	9
17574	2015-01-10	18.6	Jet	315.2	9

lobe and hotspot respectively. In addition, in the case of the lobes, we can use spatially resolved images of the inverse-Compton flux to study the (projected) variation of magnetic field and electron number density in the lobes, as discussed by HC05 and Migliori et al. (2007).

1.3 This paper

In this paper we report on the results of a *Chandra* multi-cycle observing programme, carried out since the results reported by M10, targeting the inner jet of Pic A. As we shall see in more detail below, this gives a combined exposure on the source of 464 ks, nearly a factor 4 improvement in exposure time with respect to the last large-scale study of the source by HC05 (though the sensitivity is not improved by such a large factor, as the sensitivity of the ACIS-S continues to drop with time), and a factor 16 improvement in exposure time since the original analysis of the jet by W01. In addition, the new data give us a long time baseline, sampling a range of different timescales and comprising 9 epochs spread over 15 years, with which to search for temporal variability in the jet and other components of the source. We use this new dataset to investigate the spatial, temporal and spectral properties of the X-ray emission from all components of the radio galaxy.

We take the redshift of Pic A to be 0.0350 and assume $H_0 = 70$ km s⁻¹, $\Omega_m = 0.3$ and $\Omega_\Lambda = 0.7$. This gives a luminosity distance to the source of 154 Mpc and an angular scale of 0.697 kpc arcsec⁻¹. Spectral fits all take into account a Galactic column density assumed to be 4.12×10^{20} cm⁻². The spectral index α is defined in the sense $S_\nu \propto \nu^{-\alpha}$, where S_ν is the flux density, and so the photon index $\Gamma = 1 + \alpha$. Errors quoted are 1σ (68 per cent confidence) statistical errors unless otherwise stated (see discussion of calibration errors in Section 3).

2 OBSERVATIONS AND DATA PROCESSING

2.1 X-ray

As discussed in Section 1, *Chandra* has observed Pic A for a useful duration¹ on 14 separate occasions over the past 14 years, for a total of 464 ks of observing time. Details of the observations are given in Table 1.

The pointings of the observations differ, and this affects the quality of the available data on various regions of the source. The original observations (obsid 346) were pointed at the active nucleus, with a roll angle which included both lobes on the ACIS-S detector. The 2002 observations (3090 and 4369) were pointed at the W hotspot, and much of the E lobe emission was off the detector, as discussed by HC05. All our subsequent observations (2009-2014) have had the aim point about 1 arcmin along the jet in the W lobe, but roll angle constraints have been applied so that the E lobe always lies on the S3 or S2 chips, and also to avoid interaction of the readout streak from the bright nucleus with any important features of the source. Because the W lobe is generally on the S3 chip, which has higher sensitivity, and also because of the missing 2002 data, the observations of the E lobe are roughly 2/3 the sensitivity of those of the W lobe. However, the new observations are still a great improvement in sensitivity terms on the data available to HC05. The different pointing positions mean that the effective point spread function of the combined dataset is a complicated function of position, and we comment on this where it affects the analysis later in the paper.

The data were all reprocessed in the standard manner using CIAO 4.7 (using the *chandra-repro* script) and CALDB 4.6.7. The readout streaks were removed for each observation and the events files were then reprojected to a single physical co-ordinate system (using observation 12040 as a reference). The *merge_obs* script was used to produce merged events files and also to generate exposure maps and exposure-corrected (‘fluxed’) images, which are used in what follows when images of large regions of the source are presented: images of raw counts in the merged images are shown when we consider compact structure, for which local variations in the instrument response can be neglected. Spectra were extracted from the individual events files using the *specextract* script, after masking out point sources detected with *celldetect*, and subsequently merged using the *combine_spectra* script. Weighted responses were also generated using *specextract*. Spectral fitting was done in XSPEC and SHERPA.

Fig. 1 shows an exposure-corrected image of the centre of the field covered by the observations.

2.2 ATCA observations

Pictor A was observed in 2009 with the Australia Telescope Compact Array (ATCA) in three separate observations: two in 6-km configurations and one in a compact 352-m configuration, as summarized in Table 2. The Compact Array Broadband Backend (CABB; Wilson et al. (2011)) was used with a correlator cycle time of 10 s and the full 2048-MHz bandwidth (as 1-MHz channels) centred at 5.5 GHz (6 cm) and 9.0 GHz (3 cm). The primary beam of the ATCA varies from 9 arcmin to 13 arcmin full width at half-maximum (FWHM) across the full 2 GHz band at 6 cm. The overall extent of Pictor A is ~ 8 arcmin and so the source is completely

¹ We do not make use of two very short exposures taken early in the mission.

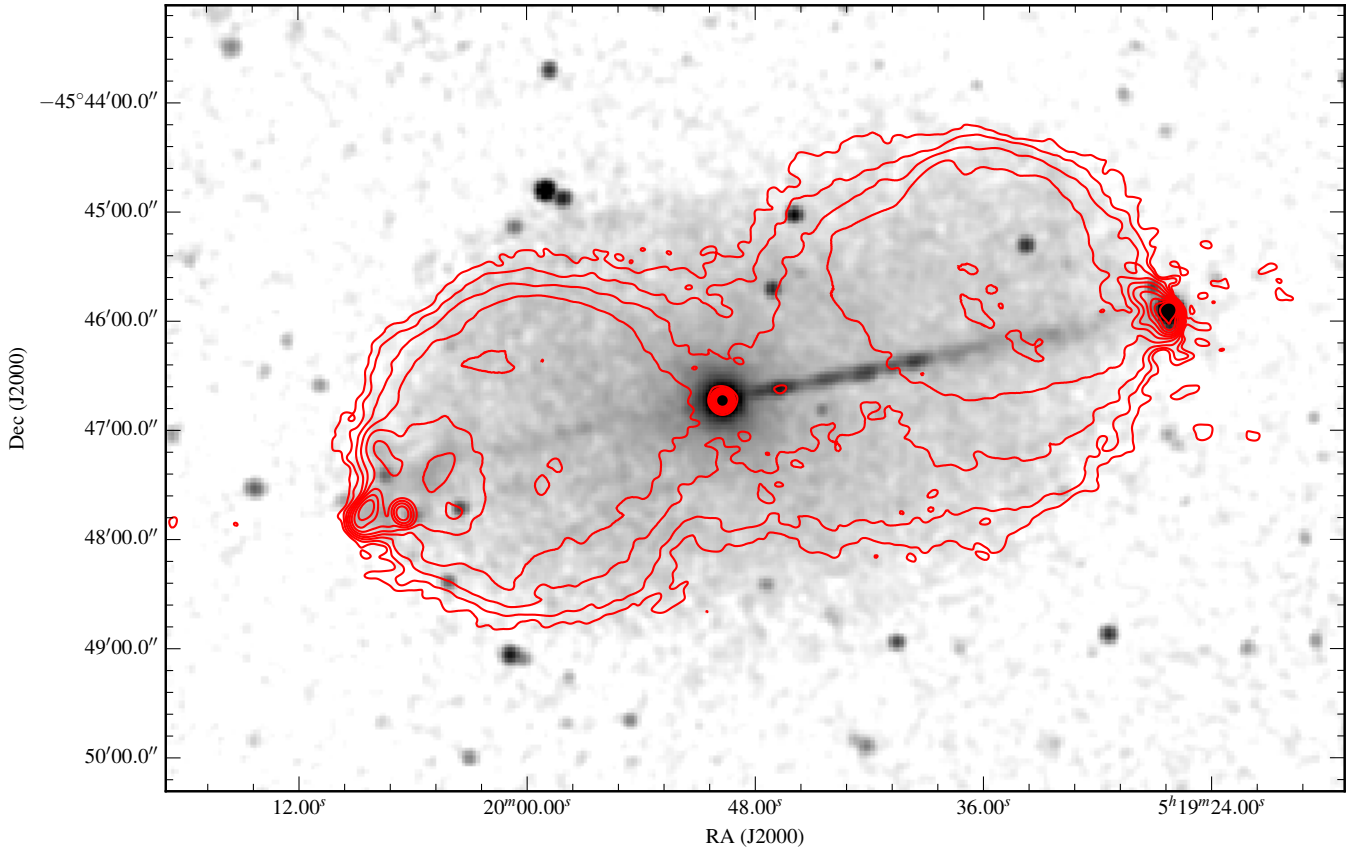


Figure 1. X-ray emission from Pictor A and its field. The greyscale shows an exposure-corrected image made from all the data in the 0.5-5.0 keV passband, smoothed with a Gaussian with a FWHM of 4.6 arcsec and with a logarithmic transfer function to highlight fainter structures. Superposed are contours of our ATCA 5.5-GHz image tapered to a resolution of 5 arcsec: contour levels are at $0.6 \times (1, 2, 4, \dots)$ mJy beam⁻¹.

Table 2. Details of ATCA CABB observations of Pictor A.

Obs. Date	ATCA config.	Central Frequency (GHz, GHz)	Time on-source (hr)
2009-06-16	6A	5.5, 9.0	12.0
2009-08-29	6D	5.5, 9.0	13.5
2009-12-06	EW352	5.5, 9.0	10.5

contained within the primary beam over the entire 6-cm frequency range. Unfortunately the 3-cm band is not of practical use as bright components of Pictor A fall outside the 6–7-arcmin FWHM of the primary beam in this band, so our results here use the 5.5-GHz data only.

The three observations, when combined using multi-frequency synthesis (MFS), provide near-complete uv -coverage spanning from 450λ out to $128 \text{ k}\lambda$. While the shortest baselines provide sensitivity to structures as large as 7.5 arcmin in extent, the longest baselines provide a resolution approaching 1.6 arcsec. In the work presented here a uv taper between 70 and $100 \text{ k}\lambda$ has been applied, giving resolutions of 1.7-2.2 arcsec, to highlight the large-scale structure of the source and to ensure that sufficient visibility data (with overlapping baselines) is available to model the spectral variation of these structures. A more heavily tapered image is used to show details of the lobes (Fig. 1).

To facilitate initial calibration, a 10 minute scan of the standard flux density calibrator source PKS B1934-638 was made at each epoch and a bright secondary calibrator, PKS B0537-441

($\alpha = 5^{\text{h}}38^{\text{m}}50^{\text{s}}36$, $\delta = -44^{\circ}5'8.94''$), was observed for 4-6 minutes every 17-20 minutes during target observations of Pictor A. While observing Pictor A, the pointing centre was set to the position of the core from earlier ATCA observations ($\alpha = 5^{\text{h}}19^{\text{m}}49^{\text{s}}75$, $\delta = -45^{\circ}46'43.80''$) so that the hot spots and lobes would be contained within the primary beam of the ATCA at 6 cm.

Primary flux density calibration, initial time dependent calibration and data flagging for radio frequency interference was performed using standard calibration procedures for the ATCA in the data reduction package MIRIAD (Sault et al. 1995). The three epochs were then combined, frequency channels averaged to 8 MHz channels. Initial imaging in MIRIAD indicated that the deconvolution algorithms available in that package were not adequate enough to deal with the complex spatial and frequency-dependent structures present in Pictor A. The visibilities were therefore exported into uv -FITS format so that they could be processed with other packages.

Initial attempts to process the data with Common Astronomy Software Applications (CASA²), where more advanced deconvolution algorithms were available, encountered issues associated with the difficulty of simultaneously deconvolving and calibrating data from an array with only a small number of baselines. This prevented the standard clean-selfcal cycle from converging towards a solution that accurately represented the source - particularly around

² <http://casa.nrao.edu/>

the hotspots where the synthesised-beam side-lobes were difficult to separate from the diffuse lobe emission.

As an alternative approach, an attempt was made to perform uv -visibility modelling of the different structures in the source. To achieve this, the data were imported into DIFMAP (Shepherd et al. 1994). DIFMAP allows components to be added and modelled in the visibility domain while also modelling for simple power-law spectral effects. The main structures of Pictor A (lobes, hotspots and lobes) were iteratively modelled (for position, size, orientation and spectral index) using a combination of Gaussian and point-like components. As more source flux was recovered in the component model, successive iterations of phase self-calibration were performed between additional iterations of component modelling. Ultimately, once a significant proportion of the source was recovered in the component model, amplitude self-calibration was also performed. At this stage it was clear that the calibration solutions at the hot spots were different to those at the AGN core. The cause of this is most likely due to pointing errors, which would shift the position of the hotspot closer and further from the FWHM of the primary beam as a function of time, and also the rotation of the primary beam over the course of an observation (the ATCA has an Alt-Az mount and so the sky rotates with respect to the feed over time). When peeling the north-west hotspot, we see a smooth increase in scatter in the gain corrections from around 1.5 per cent at the lower end of the band to 5.5 per cent at the top end of the band. While this correction encapsulates both pointing errors and primary beam rotation errors (as well as, in principle, any intrinsic variability in the source) it is reasonably consistent with what one would expect with a pointing error of ~ 5 arcsec rms, based on modelling the primary beam within MIRIAD: this is significantly better than the worst-case pointing errors of ~ 15 arcsec observed at the ATCA.

To minimize the observed position-dependent gain errors the technique known as ‘peeling’ (Intema et al. 2009) was used to generate position-dependent calibration solutions at the north-west hotspot and at the AGN core. The technique involves iteratively subtracting the sky model for everything except the direction of interest and then determining the calibration solution for that direction. One of us (EL) developed two software tools needed to do this for the ATCA data: one to subtract DIFMAP components from a DIFMAP visibility FITS file and another to compare an uncalibrated and calibrated DIFMAP FITS file to determine the gain corrections applied and then transfers these to another DIFMAP FITS file. Applying the peeling techniques improved the dynamic range of the resulting image by more than a factor of 4 and resulted in a residual off-source image noise of $\sim 40 \mu\text{Jy beam}^{-1}$. The final calibrated, modelled and restored image, which is equivalent to the zero-order term of the MFS imaging at a reference frequency of 5.5 GHz, was imported back into MIRIAD and the task *linmos* used to correct for primary beam attenuation. There is no reliable single-dish flux measurement at 5.5 GHz, but we would expect a total source flux density of 17.9 Jy based on interpolation between the Parkes catalogue flux at 2.7 GHz and the 23-GHz WMAP data (Bennett et al. 2013), or 21.8 Jy if the 1.41-GHz Parkes data is used as the low-frequency point; our final image contains 18.8 Jy, which sits well between these limits. The low-resolution 5-GHz images of Perley et al. (1997) contain 23 Jy at 4.9 GHz, implying a flux difference of order 10 per cent after correction for spectral index, but given flux calibration uncertainty and the fact that both images are significantly affected by the relevant telescope’s primary beam, we do not regard this as problematic.

The residual noise level of the final image is approximately a

Table 3. Approximate 0.5–5.0-keV counts (summed over all observations) in the key features of the radio galaxy seen in X-rays.

Component	Net counts	Error	Region used	Background
AGN	119277	345	Circle	Concentric
Jet	7077	124	Box	Adjacent
Counterjet	490	61	Box	Adjacent
W hotspot	32464	182	Circle	Concentric
E hotspot	2092	105	Ellipse	Concentric
Lobes	40537	790	Ellipse	Concentric

factor of 5 higher than the estimated thermal noise for this observation but still provides the highest dynamic range (46000:1) yet achieved for this complex source. Further gains could potentially be obtained with improved modelling and peeling of the north-west hot spot, as the highest residual errors are still concentrated on this region. Such improvements, however, are not required for the present analysis.

We have verified that the ATCA radio core, with a position in the new images of $05^{\text{h}}19^{\text{m}}49^{\text{s}}724$, $-45^{\circ}46'43.86''$, is aligned with the peak of the *Chandra* emission from the active nucleus to a precision of better than 0.1 arcsec; accordingly, we have not altered the default astrometry of the *Chandra* and ATCA images. There may well be some small astrometric offsets in the *Chandra* data far from the aim point, which would effectively blur or smear the *Chandra* PSF on these scales, but we see no evidence that they are large enough in magnitude to affect our observations. Our radio core position is in good agreement with the VLBI position of $05^{\text{h}}19^{\text{m}}49^{\text{s}}7229$, $-45^{\circ}46'43.853''$ quoted by Petrov et al. (2011).

2.3 Other data

The radio data of Perley et al. (1997) were kindly made available to us by Rick Perley. The high-frequency, high-resolution VLA images do not show the radio core (we have only images of the two hotspots, sub-images of a larger image which is no longer available) and so we cannot align them with the X-ray data manually, but the hotspot images do not show any very large discrepancy with the ATCA data on visual inspection. Perley et al. (1997) quote a core position from the short baselines of their BnA-configuration X-band data which in J2000.0 co-ordinates is $05^{\text{h}}19^{\text{m}}49^{\text{s}}693$, $-45^{\circ}46'43.42''$, 0.55 arcsec away from our best position: however, this difference does not necessarily affect all the data in the same way, and in any case the images we use are probably also shifted as a result of phase self-calibration.

Hubble Space Telescope (HST) observations of the jet were taken as part of this project, but are not described here: see Gentry et al. (2015) for details of the observations and their results. We comment on the implications of these observations for models of the jet in the discussion.

3 ANALYSIS

As Fig. 1 shows, many features of the radio galaxy are detected in X-ray emission. In addition to the bright nucleus, we see emission from the well-known jet and hotspot on the W side of the source, with the jet now seen to extend all the way to the hotspot at 250 arcsec (174 kpc in projection) from the nucleus. A jet in the E lobe (hereafter the ‘counterjet’) is now clearly detected, although much fainter than the jet, and appears to extend all the way from the nucleus to an extended region of emission associated with the E

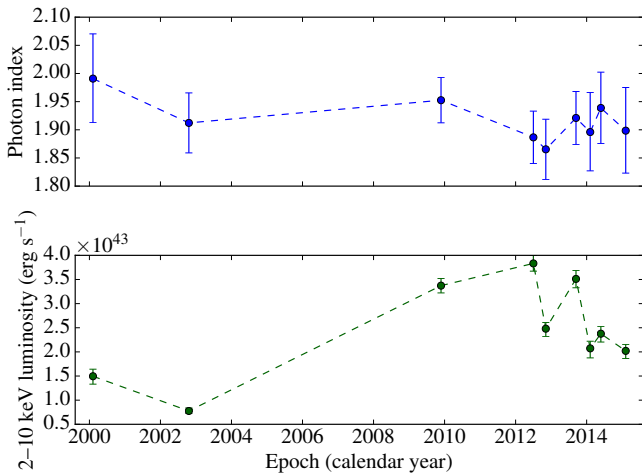


Figure 2. The best-fitting photon indices and luminosities for a single power-law model of the AGN as a function of observing date.

hotspots. Finally, the lobes of the radio galaxy are very clearly detected, presenting very uniform surface brightness in X-rays with some X-ray emission extending beyond the lowest radio contours. Table 3 lists the total number of *Chandra* counts in the combined observations in each of these features in order to give an indication of the significance at which they are detected and the degree of certainty with which we can discuss their properties.

It should be noted that the number of counts obtained for some components of the system ($> 10^4$) puts us in the regime, discussed by Drake et al. (2006), in which calibration uncertainties are likely to dominate over statistical ones. Methods to include calibration uncertainties in the analysis of *Chandra* data have been discussed by, e.g., Lee et al. (2011) and Xu et al. (2014). As the uncertainties are rarely critical to our analysis, particularly given that we construct time series for all the brightest components of the source, we do not make use of such methods, but we comment below qualitatively whenever the calibration uncertainty is likely to exceed the quoted statistical uncertainty. For a power-law fit, the typical calibration uncertainties on the photon index are $\sigma_{\text{sys}} \approx 0.04$ (Drake et al. 2011).

In the following subsections we discuss the properties and origins of each of the X-ray features, comparing with data at other wavelengths where appropriate. Table 4 gives a summary of the properties of X-ray spectral fits for discrete regions of the combined X-ray dataset.

3.1 The AGN

The emission from the AGN is strongly piled up in the *Chandra* observations and so our data are not particularly useful for studying it in detail. However, we can obtain some information about AGN variability over the period of the observations.

To deal with the effects of pileup we extracted spectra from annular regions (as used by e.g. Evans et al. 2004) covering the wings of the AGN point spread function (PSF). The annulus had an inner radius of 6.3 pixels and an outer radius of 29 pixels – the inner radius excludes all regions of the AGN emission that are piled up at more than the 1 per cent level at any epoch, while the relatively small outer radius was chosen because the observations of epoch 2 have the core close to the gap between ACIS-S and ACIS-I chips. For the same reason, the background was taken from a circular re-

gion displaced ~ 1 arcmin to the NW. The ancillary response files (ARFs) for the spectra of the annular regions were then corrected for the energy-dependent missing count fraction using point-spread functions generated using the ray-tracing tool SAOTRACE and the detector simulator MARX in the manner described by Mingo et al. (2011), using the satellite aspect solution appropriate for each observation so that the simulated and real data are as close a match as possible. (Note that the spectrum input to SAOTRACE does not affect the correction factor, which is just derived from the ratio of the counts in the annulus to the total counts in the PSF as a function of energy: a flat input spectrum was used to achieve constant signal to noise in the corrections.) The correction factors calculated are quite large for soft X-rays, ~ 40 between 0.4 and 2.0 keV, but fall significantly towards higher energies as expected.

We then fitted a single unabsorbed model³ to the spectra for each epoch, obtaining the results plotted in Fig. 2, where the 2-10 keV fluxes were obtained using the SHERPA *sample_flux* command. All fits of this model were good, with reduced $\chi^2 \sim 1$. Unsurprisingly, our results show that the AGN has varied significantly in total luminosity over the period of our observations, though any variation in photon index is much less prominent. In Table 5 we list some core photon indices and luminosities from the literature and from the available archival *XMM* data, which show that the luminosities and photon indices we obtain are very similar to those found in earlier work. In particular, the *XMM* data confirm the low luminosity seen by *Chandra* in the early 2000s but suggest that the source had returned to more typical luminosities by 2005.

The individual epochs from the annulus observations are not sensitive enough to search for Fe $K\alpha$ emission, but when we combine the corrected annulus data and fit with a single power-law model (Table 4) a narrow feature around 6 keV is seen, which can be fitted with a Gaussian with peak rest-frame energy 6.36 ± 0.02 keV, $\sigma = 50$ eV (fixed) and equivalent width 330_{-90}^{+30} eV. It is possible that this feature is itself variable (which would explain the discrepancy between our equivalent width and the upper limit set by Sambruna et al. (1999)) but our data are not good enough to test this model further.

3.2 The jet and counterjet

The radio jet of Pic A, first described by Perley et al. (1997), is a very faint, one-sided structure, hard in places to distinguish from filamentary structure in the lobes. There is no detection of the jet at wavelength between radio and X-ray, with the exception of a few knots identified in the *HST* imaging by Gentry et al. (2015); for example, it is not clearly visible in the available *Spitzer* 24- μm data. This makes the bright, knotty structure seen in the X-ray all the more remarkable, as noted by W01. Many comparable lobe-dominated, beamed systems with brighter radio jets show little or no jet-related X-ray emission in *Chandra* images (e.g. 3C 263, Hardcastle et al. 2002; 3C 47, Hardcastle et al. 2004). The counterjet is not detected at any wavelength other than the X-ray; again,

³ In models with an additional component of absorption at the redshift of Pic A, the fitted N_{H} is consistent with zero at all epochs, and a 3σ upper limit is typically $1-2 \times 10^{20} \text{ cm}^{-2}$, i.e. significantly less than the Galactic column towards the AGN. Pic A, unlike some other broad-line radio galaxies, appears in our data to be a genuine ‘weak quasar’ with an unobscured line of sight to the accretion disk. Sambruna et al. (1999) measured a slight excess absorption over the Galactic value in their *ASCA* observations, but *Chandra* has much better soft sensitivity and the *XMM* data also imply no excess absorption, so we believe our constraint to be more robust.

Table 4. X-ray spectra of discrete regions: spectral parameters and fitting statistic. Parameters given without errors are fixed in the fit. Symbols are as follows: Γ_1 , photon index of the fitted power law; Γ_2 , photon index of the high-energy part of a broken power-law model; kT , temperature of a thermal model; E_G , rest energy of a Gaussian.

Region	Model	Photon index (Γ_1)	Second parameter (photon index or energy/keV)	PL 1-keV flux density (nJy)	χ^2	d. o. f.
AGN (annulus)	PL	1.88 ± 0.01		1750 ± 20	454.3	326
AGN (annulus)	PL + Gaussian	1.90 ± 0.01	$E_G = 6.36 \pm 0.02$ keV	1760 ± 20	417.4	324
Jet (inner)	PL	1.92 ± 0.03		11.7 ± 0.2	134.5	144
Jet (outer)	PL	1.96 ± 0.09		2.9 ± 0.2	39.1	48
Counterjet	PL	1.7 ± 0.3		1.7 ± 0.3	14.3	20
W hotspot (entire)	PL	1.94 ± 0.01		90.5 ± 0.5	394.1	304
	broken PL	1.86 ± 0.02	$\Gamma_2 = 2.16^{+0.06}_{-0.04}$	90.8 ± 0.6	329.4	302
	pure thermal	–	$kT = 3.14 \pm 0.05$	–	567.8	303
	PL + thermal	2.01 ± 0.05	$kT = 4.0 \pm 0.4$ keV	63 ± 5	346.3	302
W hotspot (compact)	PL	1.97 ± 0.01		76.8 ± 0.5	418.7	283
	broken PL	1.87 ± 0.02	$\Gamma_2 = 2.23^{+0.07}_{-0.04}$	77.2 ± 0.5	341.1	281
W hotspot (bar)	PL	1.83 ± 0.03		11.5 ± 0.2	142.4	144
E hotspot (whole)	PL	1.76 ± 0.10		7.4 ± 0.4	87.5	84
E hotspot (X1, X3 excluded)	PL	1.80 ± 0.12		5.9 ± 0.4	55.3	65
Lobe (whole)	PL	1.57 ± 0.04		99 ± 1	127.4	108
Lobe (E end)	PL	1.64 ± 0.19		7.5 ± 0.9	56.4	54
Lobe (E middle)	PL	1.34 ± 0.12		30 ± 1	98.1	94
Lobe (middle)	PL	1.67 ± 0.08		25 ± 2	85.4	104
Lobe (W middle)	PL	1.75 ± 0.08		30 ± 2	112.2	105
Lobe (W end)	PL	1.54 ± 0.10		16 ± 1	84.3	96
Lobe (outside contours)	PL	2.07 ± 0.15		8.7 ± 0.4	54.6	69
	Thermal	–	$kT = 2.7 \pm 0.5$ keV	–	61.7	69
	PL + thermal	1.57	$kT = 0.33 \pm 0.07$ keV	7.1 ± 0.5	56.5	68

Table 5. Literature/archive luminosities and photon indices for the AGN of Pictor A

Date	Telescope (instrument)	Reference	Luminosity (2-10 keV, erg s^{-1})	Photon index
1996 Nov 23	ASCA	3	3×10^{43}	1.80 ± 0.02
1997 May 08	RXTE PCA/HEXTE	4	6×10^{43}	1.80 ± 0.03
2001 Mar 17	XMM PN	1	1.82×10^{43}	1.77 ± 0.01
2005 Jan 14	XMM PN+MOS	2	2.86×10^{43}	1.775 ± 0.002

References are (1) HC05 (data re-analysed for this paper) (2) Migliori et al. (2007) (data re-analysed for this paper) (3) Sambruna et al. (1999) (4) Eracleous et al. (2000), corrected to modern cosmology. Note that the *Rossi X-ray Timing Explorer* data used by reference (4) would have included contributions from the jet, lobe and hotspot regions.

continuous counterjet emission is unusual in FRIIs, although there are several examples of knots from the counterjet side being detected in narrow-line radio galaxies (Kraft et al. 2005; Kataoka et al. 2008) and there is a clear detection in at least one FRI (Worrall et al. 2010).

3.2.1 Jet X-ray structure

Fig. 3 shows an image of the jet region with radio contours overlaid. We begin by noting the following basic properties of the X-ray jet:

- As stated above, the jet extends for all of the ~ 4 arcmin between the AGN and the hotspot. However, there is a very pronounced surface brightness change at 2 arcmin, just after the knot D indicated on Fig. 3. Little or no distinct compact structure is seen after this point. Hereafter we refer to the bright structure within 2 arcmin of the nucleus as the ‘inner jet’ and the remainder as the ‘outer jet’.

- The jet is quite clearly resolved transversely by *Chandra* over

most of its length (conveniently placed point sources show the approximate size of the effective PSF at 1 and 4 arcmin from the nucleus).

- The jet broadens with distance from the nucleus. The inner jet has an opening angle of roughly 3° , which, remarkably, is also the angle subtended by the X-ray hotspot at the AGN. It is hard to say whether the outer jet has the same opening angle, but certainly most of its emission is contained within boundary lines defined by the inner jet (Fig. 3).

- There is strong variation in the surface brightness of the inner jet with distance from the nucleus, with particularly bright regions (labelled as ‘knots’ A,B,C,D) at around 30, 60, 80 and 105 arcsec from the nucleus; the quasi-periodic spacing of these ‘knots’ is striking. However, there are no locations where the surface brightness convincingly drops to zero. There is also some indication that the jet is not uniform transversely, in the sense that the brightest regions are displaced to one or the other side of the envelope defined by the diffuse emission (Fig. 3).

- Although there are radio detections of the brightest X-ray fea-

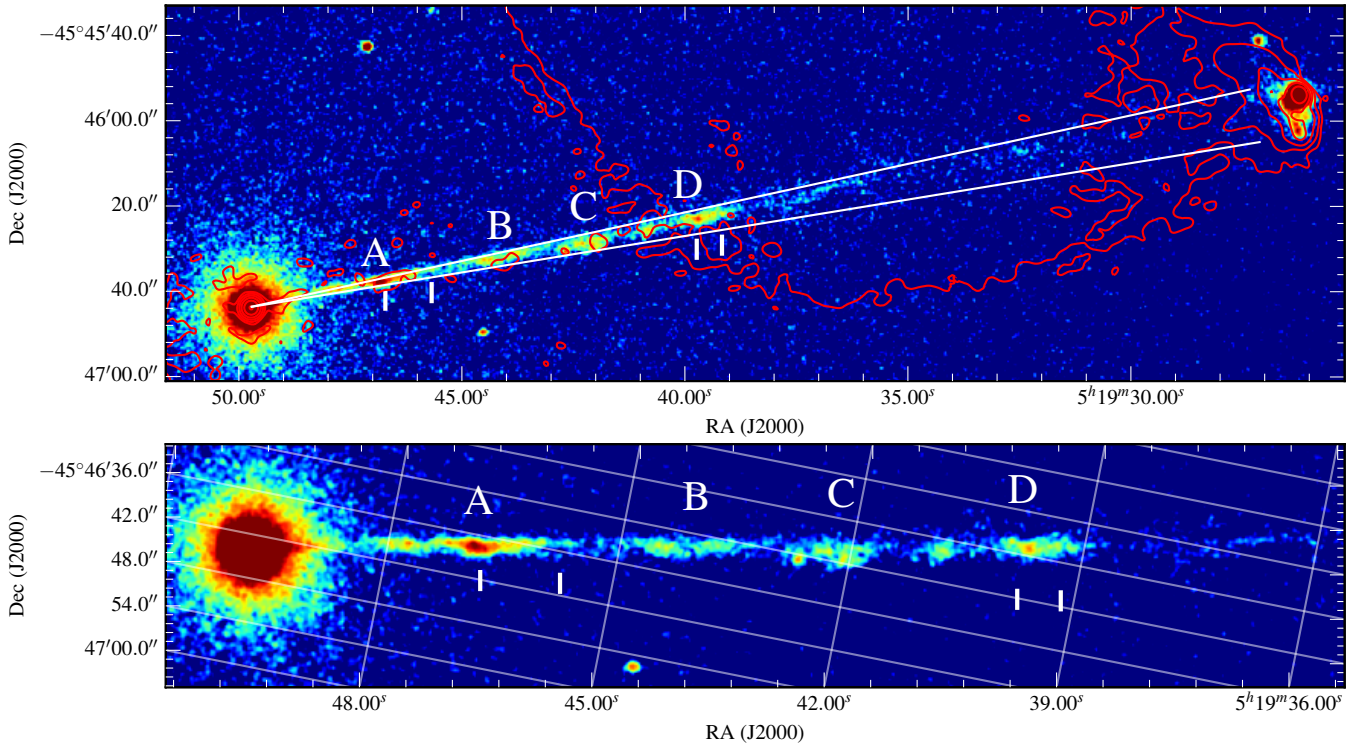


Figure 3. X-ray emission from the jet. Top panel: raw counts in the 0.5-5.0 keV band, binned into 0.246-arcsec pixels and smoothed with a Gaussian with FWHM 0.58 arcsec. Superposed are contours of the ATCA 5-GHz image with a resolution of 2.2 arcsec (contours at 1, 4, 16... mJy beam⁻¹). White diagonal lines indicate an opening angle of 3° centred on the active nucleus. White vertical lines give the positions of candidate optical counterparts. Bright regions of the inner jet are labelled for reference in the text. Bottom panel: the same data, binned in 0.123-arcsec pixels and smoothed with a Gaussian of FWHM 0.44 arcsec, rotated and zoomed in on the inner jet.

tures, the radio knots are not particularly well aligned with the X-ray features, and certainly do not match them morphologically. (However, we caution that the radio data are dynamic-range limited around the bright core, confused by structure in the lobes, and of intrinsically lower resolution than the X-ray data, so a detailed comparison is difficult.)

3.2.2 Jet X-ray and broad-band spectrum

We initially extracted spectra (Table 4) for the inner and outer jet regions separately, using rectangular extraction regions with adjacent identical background regions (which account for lobe emission adjacent to the jet) and combining data from all observations as discussed above. The 1-keV flux densities of these regions are quite different (11.7 ± 0.2 nJy versus 2.9 ± 0.2 nJy) but the photon indices are consistent (respectively 1.92 ± 0.03 – note that the error here is probably underestimated because of calibration uncertainties – and 1.96 ± 0.09). Thus there is no evidence for differences in the emission mechanisms in the two parts of the jet.

We next divided the inner jet into small adjacent rectangular regions with a length of 5 pixels (2.46 arcsec) and width 16 pixels (7.8 arcsec). These regions are wide enough that we should be looking at resolved regions of the jet and that variations between the PSFs of different observations should have little effect. Starting at 8 arcsec from the core, we extracted spectra for each region, 47 in total over the full extent of the inner jet. The results are shown in Fig. 4. We see that there is no evidence for significant changes in the jet photon index as a function of length. Only one region, a

region of low surface brightness in between knots C and D, shows weak evidence for a significantly different X-ray spectral index, unlike the case in the best-studied FRI jet, that of Cen A, where clear systematic trends in the jet photon index as a function of position are seen (Hardcastle et al. 2007a).

3.2.3 Jet emission profile

To quantify the structure seen in the images of the jet (Fig. 3) we next divided the jet up into finer regions (1 arcsec long by 10 arcsec across the jet) and fitted a model consisting of a flat background and a Gaussian to the events of each slice, using a likelihood method with Poisson statistics. We fitted only to slices detected at better than the 2σ level. The width (σ) and position of the Gaussian (in terms of its angular offset from the mid-line of the jet) were free to vary, as was the background level, which was additionally constrained by fitting to adjacent 10-arcsec regions containing no jet emission. The width of the Gaussian was combined with the expected $\sigma = 0.34$ arcsec of the un-broadened PSF to give a rough deconvolution of PSF effects. In general, we found that a transverse Gaussian gave an acceptable fit to the profile slices; there was no evidence for significant edge-brightening. However, there are clear variations in the size and offset of the Gaussians along the jet, as shown in Fig. 4. The jet gets systematically wider with length, and we see that the inner knots are systematically displaced to the N while knot C is systematically S of the centre-line (which is approximately the line between the core and the brightest part of the hotspot). The outer envelope of the jet (roughly estimated as

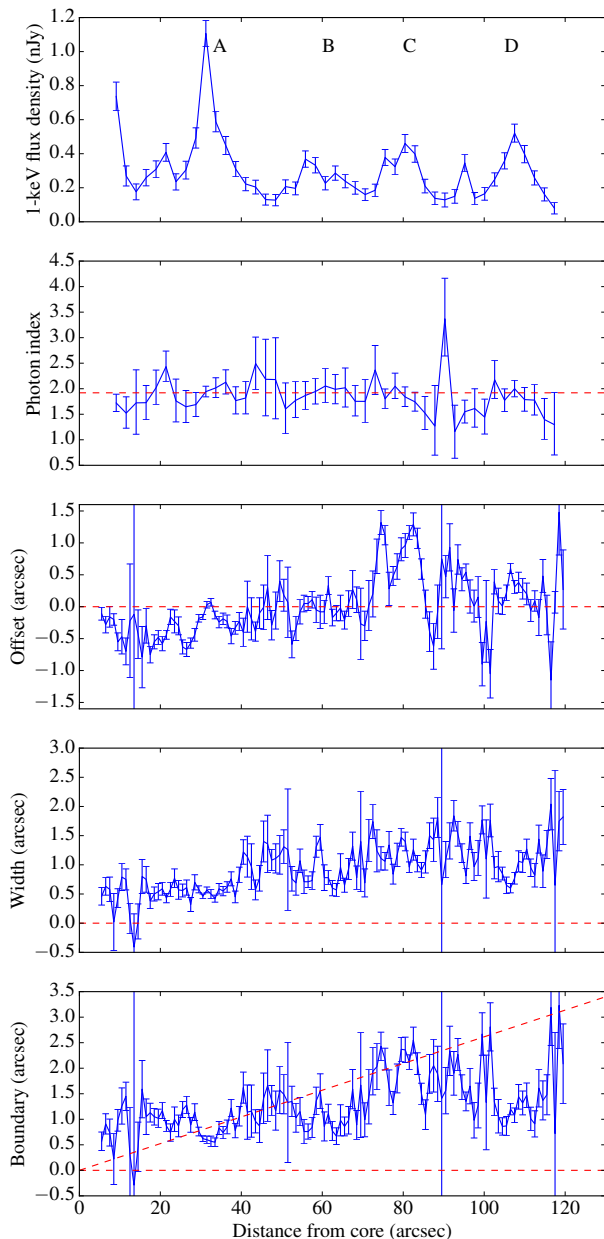


Figure 4. Profiles of various quantities along the inner, bright part of the jet. First and second panels: flux density and photon index from spectral fits to the jets. The approximate positions of the brightness peaks in the jet are labelled in the first panel, and the best-fitting photon index for the whole inner jet is plotted as a red dashed line. Third panel: transverse offsets of the centroid of the jet from the mid-line, indicated by the red dashed line. Negative offsets are in a counterclockwise (roughly northern) sense, positive ones in a clockwise (southern) one. Fourth panel: the deconvolved width (σ) of the Gaussians fitted to the transverse profile. Fifth panel: the sum of the Gaussian width and the absolute value of the offset, giving an indication (since σ is approximately the half-width at half-maximum) of the location of the outer envelope of the jet emission. The sloping red dashed line corresponds to a jet opening angle of 3° . Note that the 1-arcsec widths of the slices used in panels 3-5 means that adjacent data points are not completely independent. See the text for more details on the construction of the profiles.

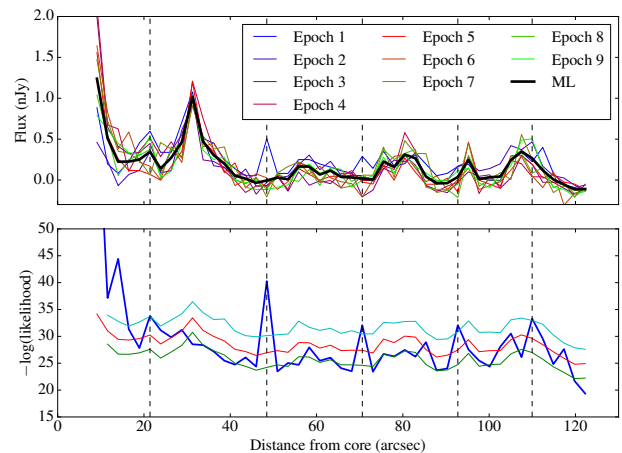


Figure 5. Profile of the flux density as a function of epoch (top) and the negative log-likelihood of the best-fitting constant-flux model (bottom) along the inner jet. See text for a description of the points. The top panel is colour-coded by observing epoch, with the thick dark blue line giving the maximum-likelihood flux density on the assumption of a constant flux across all epochs as a function of the position of the extraction region: error bars are not plotted for clarity. The bottom panel shows the log-likelihood for the fit at that position as the thick blue line and the expected value and 90 per cent and 99 per cent upper bounds as thin green, red and cyan lines respectively.

the sum of the Gaussian width and its offset) also gets larger with distance from the core, and it can be seen that at large distances the envelope is roughly consistent with a constant opening angle around 3° . At distances $\lesssim 20$ arcsec from the core the jet appears to be slightly resolved with a constant Gaussian width of about 0.5 arcsec.

The analysis we have carried out is very similar in intention and methods to the analysis of the radio data for the straight jets of four powerful lobe-dominated quasars by [Bridle et al. \(1994\)](#), so it is interesting to compare our results with theirs. Like us, they see a roughly linear increase of jet width with length in two sources with very well-defined straight jets (3C 175 and 3C 334). The opening angles in these jets are similar to those seen in Pic A ($2-3^\circ$). Having said that, the two other quasars they study in detail show little or no trend with distance, and there is some evidence that 3C 334 recollimates at large distances, so it is not clear that all these jets can be expanding freely over their length. We return to the implications of the apparent constant opening angle in Pic A below, Section 4.1.3.

3.2.4 Jet variability

To assess the level of variability in the jet we used the same regions as in the previous section, but now divided into the 9 epochs of observation listed in Table 1. There are not enough counts in each region after this division to allow fitting of models to the extracted X-ray spectra as a function of time in XSPEC or SHERPA, even with fixed photon index; moreover, the errors on the counts in individual regions are quite high if the adjacent local background regions are used. We therefore used the following procedure:

- We determined for each epoch a background level in counts by amalgamating all background regions at more than 30 arcsec from the core, having verified that there are no systematic trends in

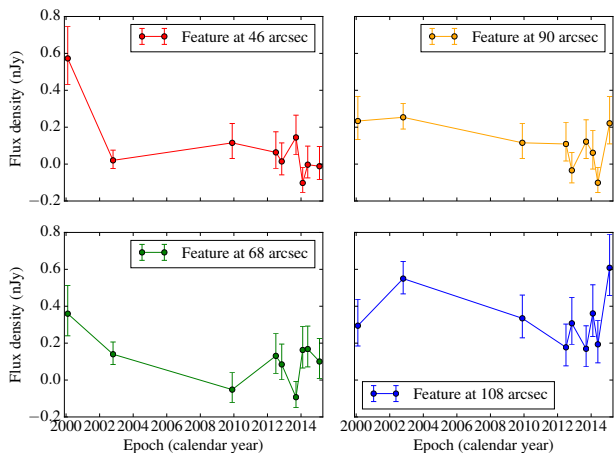


Figure 6. Light curves for potentially variable features identified by the maximum-likelihood analysis. Error bars are plotted using the methods of Gehrels (1986).

the background level as a function of distance from the core at any epoch. The statistical errors on these background levels are negligible compared to the Poisson errors on counts in individual regions.

- We computed the conversion factor between 1-keV flux density and 0.4-7.0 keV counts for each region and epoch, using the response files generated to measure the photon indices shown in Fig. 4 and a fixed photon index corresponding to the best-fitting value for the inner jet. These conversion factors generally vary little with distance along the jet for a given epoch, and are featureless apart from the effect of CCD node boundaries, but of course vary quite significantly between epochs. The conversion factors allow us to plot the best estimate of the flux density profile at each epoch (Fig. 5).

- With these conversion factors and the background levels we can compute the maximum-likelihood flux density for each region on the assumption of a constant flux at all epochs: essentially this is the same approach as used in the Cash statistic for model fitting (Cash 1979). Low values of the maximum likelihood (equivalently, high values of the natural log of the reciprocal of the likelihood, plotted in Fig. 5) imply a poor fit of a constant-flux model.

From Fig. 5 it can be seen that there are several peaks in the profile of the fitting statistic, corresponding to the flare reported by M10 at 48 arcsec and the possible feature at 70 arcsec as well as to other locations. To assess the significance of these variations we determined the expected log-likelihood if the data were in fact consistent with the best-fitting constant-flux model (green line on Fig. 5): we used Monte Carlo methods to do this, taking account of the Poisson errors on the counts in each bin, though it could be done analytically. The problem of significance now in principle reduces to a classical likelihood ratio test, but since there are few counts per bin we chose not to make use of the fact that the asymptotic distribution of the log of the likelihood ratio is the χ^2 distribution: instead we computed confidence levels at the 90 and 99 per cent levels by running the Monte Carlo simulations many times to assess the distribution of the log-likelihood per bin. Setting aside the inner part of the jet, where the apparent variability is probably dominated by the AGN (we have made no attempt to subtract the wings of the PSF), we see peaks at better than 99 per cent confidence (before accounting for trials) at 22, 48, 70, 92 and 110 arcsec; by far the

most significant feature is the original flare of M10 at 48 arcsec (34 kpc in projection). Given that the variability of the core might still affect the inner jet at 22 arcsec – the plot shows a systematic downward trend of the maximum likelihood inside ~ 40 arcsec, which is plausibly due to core contamination – we suggest that only the regions beyond this point should be taken at all seriously: it is notable that three out of four of the potentially variable sources beyond 22 arcsec lie in inter-knot regions of the jet (between A and B, B and C, and C and D respectively). Light curves for these variable regions are shown in Fig. 6.

It is clear that no new flares comparable to the one reported by M10 have taken place, though we may be seeing lower-level variability in other parts of the jet. Of course, we cannot claim a 99 per cent confidence detection of variability in any other individual region because we have carried out ~ 40 independent trials, which reduces the individual significance, but the fact that we have more than one region above the 99 per cent confidence limit increases the probability that at least some of them are real. Further Monte Carlo simulation shows that the expected average number of spurious ‘detections’ over the whole jet beyond 20 arcsec at the 99 per cent confidence level derived as above, on the null hypothesis of no actual variability, is 0.46 (very similar to the level expected on a naive analysis), compared to the 5 detections reported above; there is a 37 per cent chance that one such detection is spurious, an 8 per cent chance that two are, and only a 1 per cent chance that three are spurious, so it seems very likely that some of the newly detected variable regions are real, though we cannot say which. We can rule out the possibility that the apparent variability is produced by some global *Chandra* calibration error, since this would be expected to produce correlated variability between points at the same epoch, which is not observed; as noted above, there is no evidence for small-scale features in the point-to-point count-to-flux conversion factors.

We comment on the implications of the results on jet variability in Section 4.1.2.

3.2.5 The counterjet

The counterjet is much fainter than the jet and is detected at high significance for the first time in these observations. It is not visible very close to the nucleus, and merges into the diffuse emission associated with the E hotspot. It is notable that it does not align with the brightest radio structures in that hotspot, though it does point towards a bright X-ray feature (see below, Section 3.4).

We extracted a spectrum for the detectable part of the counterjet, using a rectangular region of length 113 arcsec and height 16 arcsec centered in the E lobe and avoiding the diffuse emission around the E hotspot, again with local background subtraction. We find a 1-keV flux density of 1.6 ± 0.3 nJy and a photon index of 1.7 ± 0.3 . Thus we see no evidence from the X-ray spectrum that the jet and counterjet have different emission mechanisms.

We carried out the same profiling analysis as described in Section 3.2.3 for the counterjet, but most regions were too faint to be fitted even with large (5-arcsec) regions. There is some evidence that the counterjet is slightly broader at larger distances from the core, but the error bars are large.

3.3 The western hotspot

Fig. 7 shows an overlay of the *Chandra* and radio images of the W hotspot.

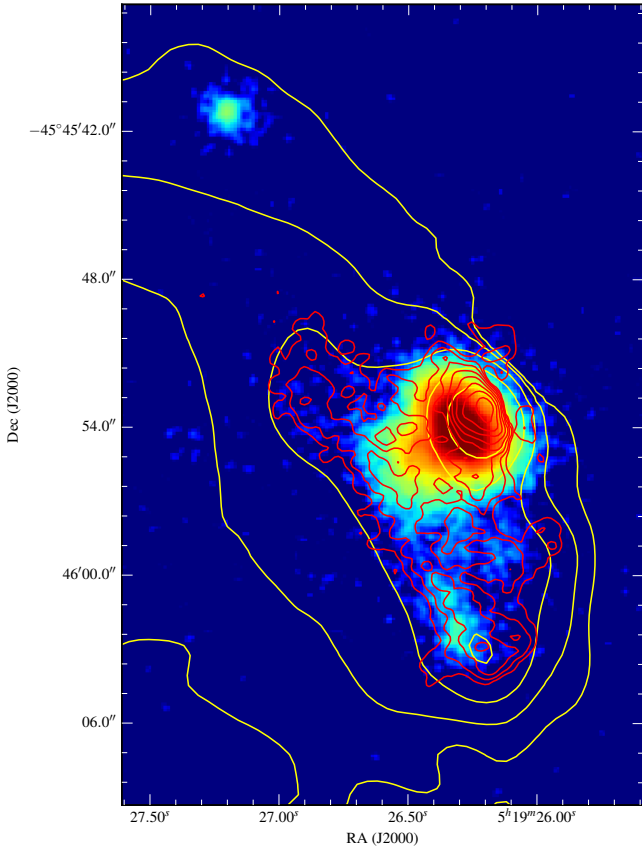


Figure 7. The W hotspot. Logarithmic colour scale shows counts in the 0.5–5.0 keV passband, binned to pixels of 0.123 arcsec on a side and smoothed with a Gaussian of $\sigma = 1$ pixel to give an effective resolution of ~ 0.7 arcsec. Overlaid are contours from the 5-GHz ATCA map with 1.7-arcsec resolution at 2,8,32... mJy beam $^{-1}$ (yellow) and contours from the 15-GHz VLA map of Perley et al. (1997) with 0.5-arcsec resolution at 1,2,4... mJy beam $^{-1}$ (red). A presumably unrelated X-ray point source to the N of the image gives an indication of the effective PSF of the stacked *Chandra* data.

We begin by noting that the high count rate in the hotspot is not necessarily wholly beneficial – for the count rates in the epoch 2 observations, where the hotspot is at the aim point, there is some possibility of pileup given the count rates of ~ 0.2 s $^{-1}$. We see no evidence of significant grade migration in the data for these epochs, probably because the hotspot is resolved (see below) and so do not attempt to correct for pileup in any way. The possibility of a small pileup effect (leading to a harder spectrum) should be borne in mind in the interpretation of our results.

W01 remarked on the strong similarity between the radio through optical morphology as seen by Perley et al. (1997) and the X-ray, and these deeper data confirm that, though they also point to some interesting differences. The most striking is a clear offset of around 1 arcsec (0.7 kpc in projection) between the peak radio and X-ray positions of the hotspot, in the sense that the X-ray emission is recessed along the presumed jet direction; this offset is visible when comparing to both ATCA and VLA data (which, by contrast, appear well aligned with each other) and is clearly real so long as our astrometry is reliable (see above, Section 2.2). Similarly, the extension of the hotspot to the SE is not so prominent in the radio or optical data, and the surface brightness distribution of X-ray and 15-GHz radio is rather different in the ‘bar’ to the E of the

compact hotspot. The X-ray bright part of this bar region, directly S of the peak X-ray emission, is consistent with being unresolved transversely by *Chandra*.

The integrated spectrum of the entire hotspot region, using a circular aperture of radius 10 arcsec which encompasses all the emission, can be fitted with a power law with $\Gamma = 1.94 \pm 0.01$ – note the similarity to the jet photon index – and total 1-keV flux density 90.5 ± 0.5 nJy. However, the fit is not particularly good (Table 4). A better fit is obtained with a broken power law, with a break energy of 2.1 ± 0.2 keV and photon indices below and above the break of 1.86 ± 0.02 and $2.16^{+0.06}_{-0.04}$ respectively, and an almost identical 1-keV flux density⁴. A pure thermal model for the hotspot is conclusively ruled out, with $\chi^2 = 567/303$ even when the metal abundance is (unrealistically) allowed to go to zero. A model with a power law and APEC thermal model (with abundance fixed to 0.3 solar, since otherwise abundance and power-law normalization are degenerate) is a less good fit than the broken power law (Table 4).

To investigate whether the broken power-law best fit is the result of the superposition of two different spectra, we divided the hotspot into non-overlapping ‘compact’ and ‘bar’ components, where the ‘compact’ region is an ellipse around the brightest part of the X-ray hotspot and the ‘bar’ region is a rotated rectangle encompassing the linear structure seen in radio emission to the E. Interestingly, these two regions do have different photon indices on a single power-law fit (1.97 ± 0.01 and 1.83 ± 0.03 for the compact and bar regions respectively: in *comparing* the two photon indices we may neglect the calibration uncertainties since the two regions have essentially the same calibration applied). However, the single power-law model remains a poor fit to the compact region and once again a broken power law is better (Table 4), with $E_{\text{break}} = 2.14^{+0.23}_{-0.14}$, $\Gamma_{\text{low}} = 1.87 \pm 0.02$ and $\Gamma_{\text{high}} = 2.23^{+0.07}_{-0.04}$. This same model, with only normalization allowed to vary, is an acceptable fit ($\chi^2 = 170.0/145$) to the bar region, although the single power-law fit is better, so there is no strong evidence for spectral differences in the two components: in any case, the steepening of the X-ray spectrum appears to be intrinsic to the compact region of the hotspot.

We searched for variability in the hotspot by fitting single power-law models to the datasets from the individual epochs (using the single large extraction region) and comparing the normalization and photon index (Fig. 8). Remarkably, there is some evidence for variations in 1-keV flux density at the 5–10 per cent level on our observing timescale, which would imply, if real, that a significant fraction of the X-ray flux from the hotspot is generated in compact regions with sizes of order pc or even less. These flux density variations are reflected in variations in the total flux in the *Chandra* band, showing that they are not simply the result of the correlated variations in photon index (errors plotted on the flux curve take the variations of both parameters of the fits into account). Particularly striking is the drop in flux or flux density at the 10 per cent level between epochs 7 and 8 (a timescale of only three months). The data are not good enough to fit broken power laws to the individual datasets, and so it is unclear whether the best-fitting broken-power-law spectrum for the integrated hotspot emission is in fact simply a reflection of this apparent temporal variability. (The associated variations in spectral index are only marginally significant, particularly if calibration uncertainty is taken into account, and so we do

⁴ Note that a similar broken power-law model is an acceptable fit to the jet, though the data quality in the jet are not sufficient to constrain the break energy or to distinguish between this model and a single power law.

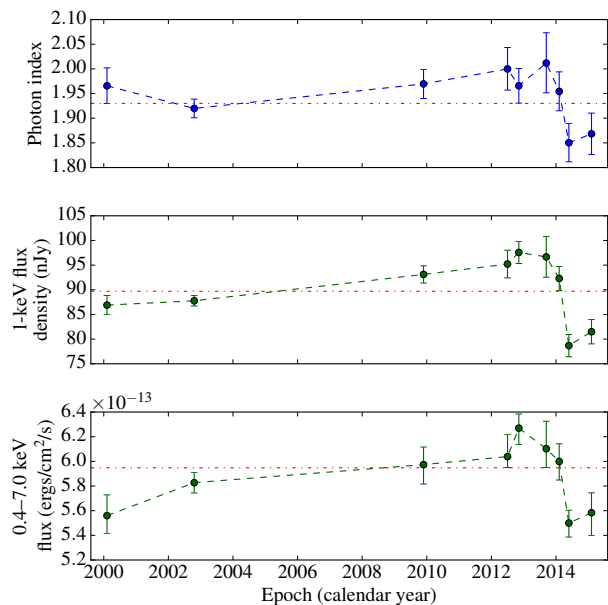


Figure 8. The best-fitting photon indices, 1-keV flux densities and total flux in the *Chandra* band for a single power-law model of the W hotspot as a function of observing date. Red dashed lines show the values derived from a joint fit to the data, effectively a weighted mean for all the observations.

not attempt to interpret them; in particular the apparently flat spectrum in epoch 2 with respect to other epochs might conceivably be an effect of pileup, as noted above, and so should not be taken too seriously.) In epoch 8 the hotspot was very close to a chip gap on the detector and, while the weighted responses that we use should take account of that, the spectrum is less trustworthy than at other epochs: however, as an essentially identical fit is found to the data for epoch 9, where the hotspot is in the centre of the ACIS-S3 chip, we are confident that the large apparent drop in flux is not an instrumental artefact. We cannot, of course, rule out some large and otherwise unknown error in recent calibration files, but it is important to note that the AGN does not show the same time variation between these two epochs (Section 3.1). On the assumption that we are seeing a real physical effect, we discuss the implications of hotspot variability in Section 4.2.

3.4 The eastern hotspot

The E hotspot is a much more complex, and much fainter structure than the W hotspot in both radio and X-ray, and accordingly we are more limited in the investigations we can carry out. A radio/X-ray overlay is shown in Fig. 9. It can be seen that essentially the whole region of excess radio surface brightness (the ‘hotspot complex’ in the terminology of Leahy et al. (1997)) is also enhanced in the X-ray, though there is not a simple relation between diffuse radio and X-ray emission (e.g. the peak of the diffuse emission in the centre of Fig. 9 is not in the same place in radio and X-ray). The relationship between the three bright compact X-ray sources (labelled X1, X2, X3 in the figure) and the two compact radio hotspots (R1, R2) is similarly unclear. X2 is clearly partly resolved in the full-resolution *Chandra* image, which makes it less likely to be a background source: if it is physically associated with the more compact radio component, R1, then the offset of 7 arcsec (5 kpc) between the

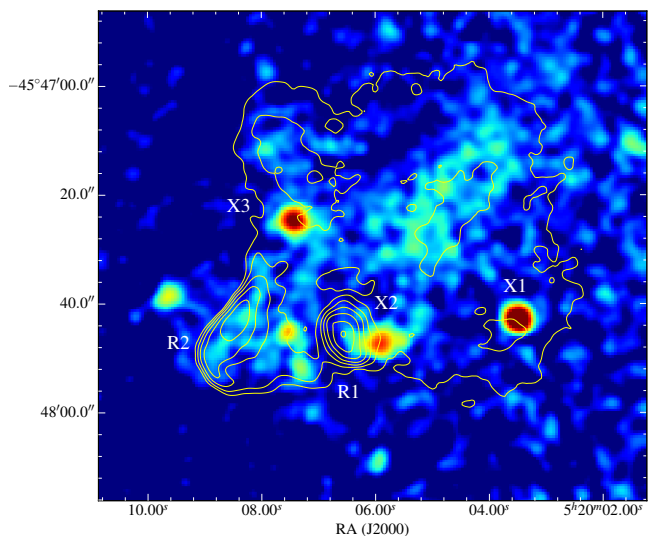


Figure 9. The E hotspot. Logarithmic colour scale shows a fluxed image in the 0.5-5.0 keV passband, binned to pixels of 0.492 arcsec on a side and smoothed with a Gaussian of $\sigma = 2$ pixel. Overlaid are contours from the 5-GHz ATCA map with 1.7-arcsec resolution at $1.5 \times (1, 2, 4, \dots)$ mJy beam $^{-1}$.

X-ray and radio peaks is significant. X1 and X3 may be background sources, but both lie at the edge of real, diffuse radio features visible in the contour map, and neither has an optical counterpart on Digital Sky Survey images. The counterjet, where last visible, points directly towards X3. There is no compact X-ray source associated with R2, but it is clearly associated with enhanced X-ray emission.

The best-fitting power-law model applied to the entire elliptical hotspot region gives a relatively flat photon index with $\Gamma = 1.8 \pm 0.1$. (The background region is a concentric ellipse, so background from the lobes is at least partially subtracted from this flux density value.) If we exclude X1 and X3, we obtain a consistent $\Gamma = 1.8 \pm 0.1$ (Table 4). Consistency of the photon index with that of the jet or W hotspot region is not ruled out at a high confidence level.

Finally, we draw attention to the apparent extension of the X-ray emission to the E and S of the sharp boundary of the radio emission at hotspot R2 (and therefore with no radio counterpart). This is not seen at high significance – the emission corresponds only to a few tens of counts – and the point source immediately to the NE of R2, which contributes to it, is surely unrelated to the radio galaxy. But it is possible that we are seeing here at a very low level shocked emission from the thermal environment of the source. There are insufficient counts to test this model spectrally, and no comparable feature can be seen around the W hotspot.

3.5 The lobes

Because the lobes are significantly contaminated by scattered hard emission from the PSF close to the nucleus, and this cannot be corrected by local background subtraction, we restrict ourselves to the energy range 0.4-2.0 keV in spectral fitting in this section⁵.

We initially carried out spectral fitting to the whole lobe region

⁵ This is more conservative than the approach used by HC05, since the AGN is substantially brighter relative to the lobes in the newer observations.

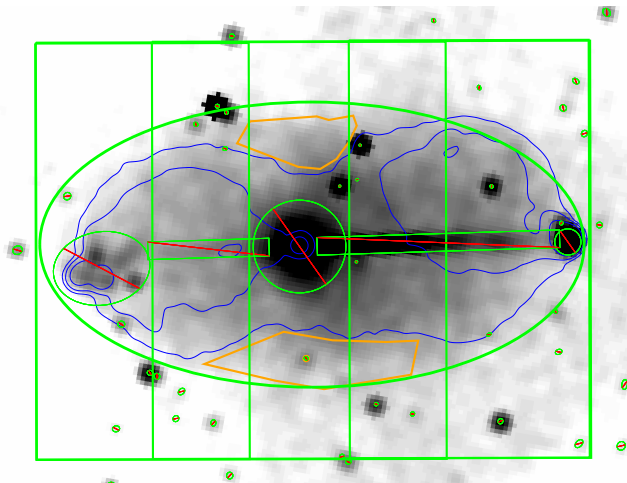


Figure 10. The regions used for lobe spectral extraction. The greyscale is a binned, smoothed image of the 0.4-2.0 keV *Chandra* counts. The large green ellipse shows the basic lobe region: the rectangles indicate the subdivision into five smaller regions for spectral fitting and the orange polygons are the extraction regions for the emission outside the radio contours discussed in the text. Exclusion regions for core, jets, hotspots and background sources are shown defaced with red lines. Also plotted (in blue) are contours from the 7.5-arcsec resolution 1.4-GHz radio map of Perley et al. (1997): contours are at 10, 40 and 160 mJy beam⁻¹.

(encompassing all of the E and W lobes with the exclusion of a 45-arcsec circle around the core and appropriate regions around the jet and hotspot) and also to a sub-division of this large region into five sub-regions in linear slices along the lobe (Fig. 10). The resulting spectrum for the whole lobe is flat ($\Gamma = 1.57 \pm 0.04$) and there is no evidence in the spectra of the sub-regions for significant variation as a function of length along the lobe, whether for physical reasons or as a result of residual contamination by the AGN (Table 4). The 1-keV flux density and spectral index we obtain are in reasonable agreement with those reported by HC05, who measured spectra and fluxes from the two lobes separately; HC05’s spectra are a little steeper, but it is possible that this is a result of their use of the whole 0.4-7.0 keV band for spectral fitting, as the inverse-Compton spectrum is expected to steepen across the *Chandra* band.

A conspicuous feature of the X-ray ‘lobe’ emission is that it extends further than the radio contours at the centre of the source: this can be seen in both Fig. 1 and Fig. 10. We do not believe that this emission is residual scattered flux from the nucleus, since, although the wings of the PSF are not negligible in this region even in the 0.4-2.0 keV energy range, the predicted surface brightness of emission from the SAOTRACE/MARX simulations described in Section 3.1 at these radii would be at least a factor 4-5 below what is observed. In an inverse-Compton model, we would always expect radio emission at some level coincident with the X-ray emission, leaving two possibilities: (1) this is genuinely inverse-Compton emission from the lobes, and so there is radio emission, but it is too faint and/or steep-spectrum to be detected; or (2) we are seeing thermal emission from the otherwise undetected hot gas halo around the lobes (which must be present at some level to confine them, and which would be expected to be particularly bright between the lobes). Possibility (1) cannot be ruled out at this point: contours of the 330-MHz images of Perley et al. (1997) do appear to include all the X-ray emission, but they are much lower in resolution than any other map we have used here (the resolution is

30×6 arcsec, with the 30-arcsec major axis being in the N-S direction) and so do not provide strong constraints. To investigate possibility (2) we extracted spectra for the regions outside the lowest contour of the L-band image shown in Fig. 10, and fitted them with thermal and non-thermal (power-law) models. The results are inconclusive (Table 4): a power-law model is a good fit to the data but with a rather steep photon index of 2.0 ± 0.1 , a thermal (APEC) model with abundance fixed to 0.3 solar fits somewhat more poorly than the power law and gives an implausibly high temperature of 2.7 ± 0.5 keV, and when we fit a combination of the two, fixing the power-law photon index to the value of 1.57 derived from the whole-lobe region, the fit is dominated by the power-law component and is no better than for the pure power-law model, though the derived temperature is more reasonable for a poor environment. Similar results are obtained from a powerlaw plus thermal fit to the middle lobe region. While we cannot rule out the possibility of some soft thermal emission, with a temperature consistent with being the environment of the host elliptical, contributing to the observed X-rays in this region, we see no compelling evidence that it is detected. High-fidelity low-frequency radio maps will be needed to test possibility (1) further.

HC05 have already discussed the evidence for large-scale variation in the X-ray to radio ratio across the lobes, and we do not repeat their analysis here. Fig. 1 already shows that any large-scale surface brightness variation in the X-ray lobes is much smaller than that in the 1.4-GHz radio emission. However, one thing that we can do with the larger volume of data available to us is to study the radio/X-ray ratio in a statistical way. As discussed in Section 1.2, the objective here is to test models for the origins of the ‘filaments’ that appear to dominate small-scale surface brightness variation in the radio lobes. In the extreme case in which the variation in synchrotron emissivity that they imply is purely due to variations in the normalization of the electron energy spectrum, with a uniform magnetic field strength, then we would expect a one-to-one relationship between the radio and X-ray emission. (This model already seems to be ruled out by the observations of HC05, though we comment on it more quantitatively below.) If, on the other hand, the variation in synchrotron emissivity is only due to point-to-point variations in magnetic field strength, with a uniform electron population filling the lobes, then we would see a uniform X-ray surface brightness (modulo line-of-sight depth effects) and thus little correlation between the radio and X-ray emission. In between these two extremes lie a range of models in which the local electron energy spectrum normalization depends on magnetic field to some extent.

To search for correlations between radio and X-ray we measure radio flux densities, and X-ray fluxes, from as large a number of discrete regions of the lobe as possible. Because we wish to search for counterparts of the filamentary structures seen when the lobes are well resolved, we use the highest-resolution radio map available to use that does not resolve out lobe structure, the 7.5-arcsec resolution 1.4-GHz map of Perley et al. (1997) (Fig. 10). Ideally we would work at even lower frequencies, since the electrons responsible for the observed inverse-Compton emission emit at 20 MHz for a mean magnetic field strength of 0.4 nT (Section 4.3), but high-resolution, high-fidelity images of the Pic A lobes at frequencies of tens of MHz will require the low-frequency component of the Square Kilometer Array (SKA): as noted above, the lowest-frequency images of Perley et al. (1997) are not good enough for our purposes. It is therefore important to bear in mind that some structure in the image can come from differences in the radio and

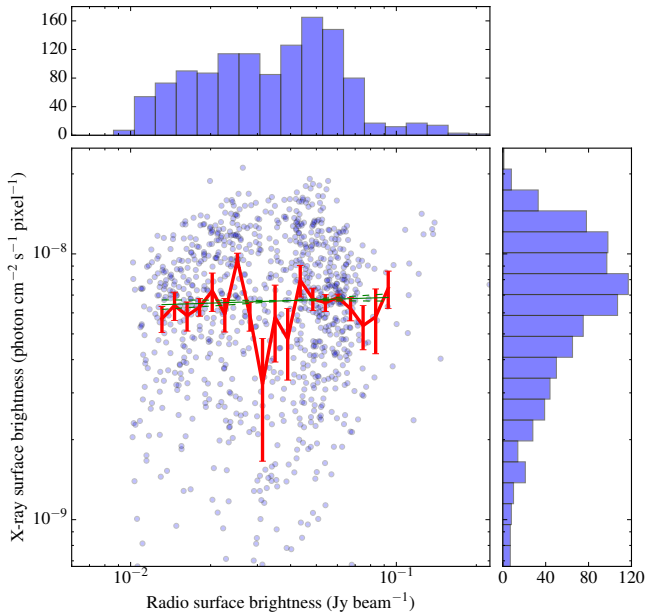


Figure 11. Relationship between radio and X-ray surface brightness (0.4–2.0 keV) in the lobes of Pic A. In the scatter plot at the bottom left, blue points show independent data points as discussed in the text; red lines and error bars show an average surface brightness in bins of radio flux; the green line shows the best-fitting power law describing the median data points in red and an estimate of the 1σ error on its slope. Histograms at the top and right show the projections of the radio and X-ray surface brightness distributions respectively.

X-ray spectral slope, and we comment on this in more detail below⁶.

To assess the relationship between X-ray and radio surface brightness we generated a fluxed X-ray image in the 0.4–2.0 keV band, exposure-corrected at 1 keV and with 2-arcsec pixels, and convolved it to a resolution matching that of the radio image. The 1.4-GHz radio and X-ray images were then regridded to the same resolution. A mask was applied to the X-ray image to exclude the core, jets, hotspots and background point sources, and the radio contour at 10 mJy beam⁻¹ was used to define the edge of the lobes. Finally, the image was sampled in distinct regions of 4×4 pixels (8×8 arcsec), taking account of masking, to ensure that each data point was independent (this is the approximate area of the convolving Gaussian for both images). Fig. 11 shows the relationship between radio and X-ray surface brightness derived in this way, and, as can be seen, there is little or no correlation between them – the X-ray surface brightness seems to be independent of the radio, and to be peaked around a value of $\sim 10^{-8}$ photons cm⁻² s⁻¹ pixel⁻¹, though with significant scatter⁷, over an order of magnitude variation in radio. This can be seen more clearly if we take the

⁶ The lack of a strong correlation between spectral index and surface brightness in the maps of Perley et al. (1997) means that it is difficult to construct a model in which *all* the differences between the X-ray and radio emission come from this difference in the electron energies being probed by the two emission mechanisms, as discussed by HC05.

⁷ Scatter in this plot can be the result of statistical noise (Poisson errors) on the X-ray emission, or dispersion with a physical origin in the radio or X-ray surface brightness, or both. As it is not easy to distinguish between the various sources of dispersion, we do not consider the magnitude of dispersion in our analysis.

median X-ray surface brightness in bins of radio surface brightness, as shown in Fig. 11. Here we take only the central 80 per cent of the data in terms of radio surface brightness to avoid edge effects and structures around the jet/hotspot, medians are used for robustness to e.g. unmasked outlier points, and errors on the median are derived using bootstrap (which takes account of both Poisson errors on individual data points before smoothing and the intrinsic dispersion within a bin). Clearly there is little correlation even after averaging: the best-fitting power-law relationship for the binned data points, also plotted in Fig. 11, has a power-law index $p = 0.047 \pm 0.038$. Models in which the electron energy spectrum is constant and the surface-brightness variation in radio emission are the result of electron density variations only are conclusively ruled out. We will discuss the implications of this analysis further in Section 4.3.

4 DISCUSSION

4.1 The jet and counterjet

4.1.1 Spectrum

For the first time we have been able to construct a detailed spectral profile of the X-ray emission from the jet (Section 3.2.2, Fig. 4). What is remarkable about this is the uniformity of the spectrum. The photon index does not deviate significantly from its mean value of ~ 1.9 for all of the 4 arcmin (~ 150 kpc in projection) over which the jet is observed. This is strong evidence that the dominant emission mechanism is the same everywhere in the jet. As noted by HC05, the steep X-ray spectrum is difficult (though not impossible) to reconcile with an inverse-Compton model for the X-ray emission, since in the beamed inverse-Compton model the electrons that produce the X-ray emission have very low energies, much lower even than those producing radio synchrotron emission, and would be expected to have an energy spectrum which would be set by the acceleration mechanism: the radio spectral index of the lobes is flatter than 0.9, as indeed is the 1.4 to 5.5-GHz spectral index of the jets where it can be estimated (~ 0.7) and the radio-optical spectral index (see Gentry et al. 2015), so an inverse-Compton model of the X-ray emission would require the acceleration process to produce an electron energy spectrum that was steep at low energies ($\gamma \ll 1000$) and flat at intermediate energies ($\gamma \sim 10^4$).

4.1.2 Jet variability

Our programme of jet monitoring has not revealed any new variability as significant as that reported by M10. It is of course a concern that the feature most consistent with a short-duration flare appears to have happened in the very first *Chandra* observation, when the ACIS-S was significantly more sensitive in the soft band than it now is. (As Fig. 6 shows, the other three, less significant regions that may be varying in the inner jet are associated with a broad scatter in the measured flux density as a function of time rather than a flare at a single epoch.) If we assume that there are no instrumental explanations for the lack of flares, then we must conclude that flares at the level reported by M10 are rare.

Our monitoring campaign does increase the evidence for temporal variation of the X-ray emission in the jet, given the several locations of moderately significant variability seen in Fig. 8. As discussed by M10, the radiative loss timescales for synchrotron-emitting electrons seem too long to be relevant to the timescales of the variation that we see (months to years) although this analysis relies on assumptions about the magnetic field strength in the jet

that cannot be substantiated at present. If the flaring mechanism is particle acceleration in compact regions followed by adiabatic expansion, then in principle similar timescales would be seen whether the emission mechanism is synchrotron or inverse-Compton emission, though the synchrotron timescales would be shorter because of the effect of expansion on the magnetic field.

4.1.3 Jet-counterjet ratio and beaming speed

With a clearly significant detection of the counterjet (Section 3.2), the jet-counterjet ratio is well constrained at 6.9 ± 1.2 (Table 4), consistent with the value reported by HC05. In a synchrotron model, where the X-ray emission is isotropic in the rest frame of the jet, and assuming an intrinsically similar jet and counterjet with the same rest-frame properties, we expect the jet-counterjet ratio to be given by

$$\mathcal{R} = \left[\frac{1 + \beta \cos \theta}{1 - \beta \cos \theta} \right]^{2+\alpha} \quad (1)$$

where α is the spectral index (taken to be 0.9), θ is the angle to the line of sight and $\beta = v/c$. We can trivially solve for the projected speed in the plane of the sky, $\beta \cos \theta = 0.32$. Since $\beta < 1$ and $\cos \theta < 1$, we require $\beta \gtrsim 0.3$ and $\theta < 70^\circ$. These are in line with expectations for a broad-line FR II radio galaxy, which would be expected from the statistics of unified models to have $\theta < 45^\circ$ and from jet prominence and sidedness statistics to have apparent $\beta \sim 0.6$ (Wardle & Aaron 1997; Mullin & Hardcastle 2009). If we assume that $\theta < 45^\circ$, then $\beta \lesssim 0.5$. In the inverse-Compton model, the speed of the emitting material in the jet is constrained to be much higher ($\Gamma \gtrsim 5$, i.e. $\beta \approx 1$), the angle to the line of sight must be small (less than a few degrees) and the emission in the rest frame is anisotropic, increasing the sidedness asymmetry: even without considering the last factor it is easy to see that \mathcal{R} would be many orders of magnitude higher than is observed. A one-zone beamed inverse-Compton model is conclusively ruled out by the counterjet detection alone, unless the counterjet's emission is produced by some other mechanism (which is disfavoured by the fact that its X-ray spectrum is identical to that of the jet).

One other constraint on the jet speed may be provided by the observed opening angle of $\sim 3^\circ$ (Section 3.2.1). For a freely expanding relativistic jet with no dynamically relevant magnetic field, we expect $\Gamma\theta \lesssim 1$ where Γ is the jet bulk Lorentz factor, and θ is the half-opening angle in radians. The assumption that $\Gamma\theta = 1$ has been widely applied in blazar modelling in the past. However, recent radio studies of blazar sources indicate that $\Gamma\theta \approx 0.1$ – 0.2 (e.g., Jorstad et al. 2005; Clausen-Brown et al. 2013; Zdziarski et al. 2015; Saito et al. 2015). Bearing in mind that the angle to the line of sight of Pic A is probably $\lesssim 45^\circ$, we have the true half-opening angle $\theta \lesssim 1^\circ$; this would imply $\Gamma \gtrsim 5$ ($\beta > 0.98$) for the jet in Pic A. The apparent inconsistency between this bulk speed and the constraints provided by the jet sidedness analysis above may be resolved if the jet's dynamics are dominated by a highly relativistic spine and its emission by a slow-moving boundary layer: we discuss such a model in more detail in the following subsection. Alternatively, of course, the jet may not be expanding freely – see the discussion of other quasar jets in Section 3.2.3 –, in which case the true value of Γ may be lower, or Pic A's jet may differ from those of blazars in some other way.

It is worth noting that, in contrast to the situation for many of the core-dominated quasars with bright X-ray jets, we have no *direct* evidence of highly relativistic bulk motions in Pic A on any scale: the VLBI observations of Tingay et al. (2000) imply at most

mildly superluminal motions. Further VLBI studies of this object would be valuable.

4.1.4 Jet physical structure

The arguments in Sections 4.1.1 and 4.1.3 strongly disfavour a one-zone inverse-Compton model for the jet X-ray emission. We regard such a model as untenable and do not discuss it further. We are therefore forced to the conclusion that synchrotron emission is responsible for some or all of the X-ray emission; in individual knots, this conclusion is strongly supported by the results of Gentry et al. (2015), who show that several knots can be well modelled with a fairly conventional broken-power-law radio through X-ray synchrotron spectrum.

To understand the origin of the synchrotron X-rays from the jet we need to consider carefully where the radiating material originates in FR II jets in general. It is important to note that ruling out the beamed inverse-Compton model as the origin for the X-ray emission does not rule out high bulk speeds in the jet, but merely the combination of high bulk speeds, small angle to the line of sight and plentiful low-energy electrons in the high-bulk-speed region required for beamed inverse-Compton to dominate the observed X-rays. This process may well still operate in other sources, and indeed might dominate the X-ray emission from Pictor A from a different line of sight. However, the X-ray jet sidedness seen in Pic A (and the radio jet sidedness and prominence seen in many other radio galaxies and radio-loud quasars) would imply that most of the *visible* jet emission in the vast majority of sources comes from moderately relativistic regions of the jet with $\beta \sim 0.6$ (Mullin & Hardcastle 2009). If we interpreted $\beta \approx 0.6$ as the bulk speed of a homogeneous jet, then we would have to explain how the jets decelerate to these speeds, without disruption or extremely obvious dissipation, from the $\Gamma \gtrsim 10$ implied by VLBI observations of core-dominated quasars, or even the Γ of a few implied by core prominence variations; we know of no mechanism that can do this. It is much more natural to consider $\beta \approx 0.6$ (suggestively close to the sound speed in an ultrarelativistic plasma) as the characteristic speed of a slow-moving boundary layer which dominates the emission, while emission from a fast central spine with $\Gamma \gtrsim 10$ (a) is suppressed by Doppler de-boosting, at least in radio galaxies and lobe-dominated quasars and (b) may in addition have a substantially lower rest-frame emissivity. This model (which has been invoked in the literature previously, see e.g. Bridle et al. 1994; Stawarz & Ostrowski 2002; Hardcastle 2006; Jester et al. 2006; Mullin & Hardcastle 2009) has the desirable feature that it does not require the whole jet to decelerate to moderately relativistic speeds until the jet termination shock at the hotspot, allowing the interpretation of hotspots as jet termination shocks even if the jet equation of state is ultrarelativistic. It also helps to explain the few observations of edge-brightening in FR II jets (e.g. Swain et al. 1998), and the fact that FR II jets have polarization-inferred *B*-field pointing along the jet direction (a natural consequence of shear even if there is a toroidal field structure in the fast spine). In Pic A, a boundary layer model is consistent with the low-filling-factor, non-centrally-brightened appearance of the X-ray jet, and such a model allows us to reconcile the observed opening angle with the constraints on its Doppler factor from a sidedness analysis, although we do not regard this latter point as a particularly compelling argument since we cannot say whether the jet is really unconfined.

In what follows, we consider various possible origins for the X-rays based on the boundary-layer model. One consequence of this model is that the effective jet volume is smaller than its physical

volume (as some of the physical volume is filled with fast-moving, Doppler-suppressed jet material which we do not (yet) see in any waveband) and so equipartition magnetic field strength estimates are lower than they should be; but even the field estimates used by M10 for the whole jet clearly require an in situ acceleration process for the particles responsible for the synchrotron X-rays. We investigate the properties required for this acceleration process in the next subsection.

4.1.5 Clues to the acceleration process

We begin by considering the energetics of acceleration. Based on a very crude broken-power-law model of the radio through X-ray jet spectrum, the total (observed) radiative jet power is of order 2×10^{35} W, or 2×10^{42} erg s⁻¹ (a number which is uncertain by a factor of a few in either direction because of the unknown Doppler factor of the emitting part of the jet within the constraints imposed by the sidedness analysis of Section 4.1.3). From the results of Mingo et al. (2014) for powerful 3CRR sources, we might expect the jet kinetic power to be of order the bolometric AGN power, which is a few $\times 10^{44}$ erg s⁻¹ (Section 3.1, assuming a bolometric correction from the X-ray of ~ 20). Mingo et al. (2014) use estimates of the jet power from the method of Willott et al. (1999), but the correlation they see between AGN power and jet power has the merit of averaging over many objects. Alternatively, we can directly use the Willott et al. (1999) estimate based on the total radio luminosity of Pic A, which gives a jet power of $\sim 2 \times 10^{45}$ erg s⁻¹ if normalized as described by Hardcastle et al. (2007a), though such estimates depend strongly on the (unknown) source environment and age (Hardcastle & Krause 2013). Given the rough consistency of these jet power estimates, we are looking for a mechanism which extracts perhaps 0.1 per cent of the energy transported by the jet and places it in synchrotron-radiating electrons, predominantly in a slow-moving boundary layer.

Our observations of Pic A give us some clues about the detailed particle acceleration mechanism. The flaring behaviour seen by us and by M10 requires the flaring regions to be small (sub-pc), although the jet is resolved by *Chandra* and therefore several kpc in diameter. A model in which the observed jet is a boundary layer alleviates this discrepancy, since the boundary layer may be much thinner than the observed diameter of the jet, but we still require either particle acceleration on small scales or rapid adiabatic compression and expansion of small regions.

Models in which the observed jet emission is a boundary layer make it somewhat easier to explain the strong variations in jet prominence both internally to a source (as in Pic A) and within sources, which in this picture would arise as a result of weaker or stronger interactions between the invisible ‘beam’ carrying most of the power and its external environment, causing more or less local acceleration in the boundary layer. In Pic A, we can speculate that the sudden reduction in X-ray emissivity about half-way along the jet may be a result of the jet moving from an environment where it is in contact with the external thermal environment to one where it is embedded in the lobes. This would not cause a significant change in the pressure external to the jet (since the lobes are presumably in approximate pressure balance with the environment in which they are embedded) but might well give rise to a change in the rate of dissipation at the boundary layer. Whether that change would be expected to be quantitatively anything like what we observe in Pic A is a question that would require detailed modelling to answer. As we see no direct evidence for an X-ray-emitting environment in Pic

A, there is no direct observational support for this model other than the sudden change in jet surface brightness.

We consider some possible physical mechanisms for particle acceleration in the following subsections.

4.1.6 Shocks

First-order Fermi acceleration at shocks is the first model to consider, as it is generally thought to be responsible for the particle acceleration at the hotspots. However, the structure of the X-ray emission, with elongated regions tens of kpc in length, does not seem consistent with localized, large-scale shocks such as would be produced by e.g., reconfinement in the external medium or strong jet speed variations. In FRI jets, entrainment of dense baryonic material from the stellar winds of host galaxy stars embedded in the jet is thought to be responsible for some of the observed kpc-scale bulk jet deceleration, and Wykes et al. (2015) have recently shown that diffusive shock acceleration at the many jet/stellar wind boundaries is energetically capable of producing the observed X-rays in the case of the well-studied source Cen A, giving *distributed*, shock-related acceleration. But in Pic A and other FRII sources this cannot be the mechanism responsible for particle acceleration, since the jet X-ray emission appears on scales where there are essentially no stars, and certainly too few to intercept the required fraction of the jet energy. The remaining possibility is some distributed oblique shocking due to instabilities propagating into the jet; in principle this could help to explain the quasi-periodic spacing of the jet knots as well. We cannot rule such a model out in the absence of a high-signal-to-noise observation of the jet boundary, e.g. from still deeper radio observations, but it is not obvious how it would reproduce the small-scale flaring behaviour of the jet.

4.1.7 Shear acceleration

Shear acceleration (Stawarz & Ostrowski 2002; Rieger & Duffy 2004) would in principle be a natural consequence of the boundary layer model outlined above. However, as Stawarz & Ostrowski (2002) point out, for electrons of the energies we are discussing here the gyroradius of electrons in an equipartition field is likely to be many orders of magnitude smaller than the characteristic size scale of the shear, greatly reducing the efficiency of the process. M10 estimate an equipartition field of 1.7 nT for the jet, and though this assumes a uniformly filled cylindrical geometry, it serves to illustrate the point: if ν is the observed synchrotron frequency, then the electron gyroradius is

$$r_g = \sqrt{\frac{\nu}{2\pi}} \frac{m_e^{3/2} c}{q^{3/2} B^{3/2}} \quad (2)$$

where m_e is the electron mass, c the speed of light, and q the charge on the electron, which for $\nu = 2.4 \times 10^{17}$ Hz gives $r_g \approx 10^{13}$ m with $B = 1.7$ nT, while the jet is transversely resolved with a radius $R \sim 1$ kpc. Only if the shear layer is very thin, of order a few times the gyroradius, does shear acceleration dominate over turbulent acceleration in the jet (cf. eq. 1 of Stawarz & Ostrowski 2002). The equipartition field also depends on the geometry. If the thickness of the boundary layer is ΔR then, roughly, $B \approx B_{eq}(R/\Delta R)^{2/(p+5)}$ where p is the power-law electron energy index; thus the gyroradius also decreases as ΔR decreases. Setting $p = 2.5$ for the sake of the calculation, we can find a self-consistent value of ΔR and B which satisfies the condition $r_g/\Delta R \approx 0.3$, but this still requires $\Delta R/R \approx 10^{-9}$, a completely implausible geometry. Moreover, the

competing process, turbulent acceleration, can easily be more efficient than assumed by [Stawarz & Ostrowski \(2002\)](#); the proton number density may well be much less than they assume, giving relativistic Alfvén speeds and thus allowing the acceleration of very high-energy electrons, and requiring $r_g \approx \Delta R$ for shear acceleration to dominate, at which point the assumptions of the model break down in any case. We discuss turbulent acceleration in the following subsection.

4.1.8 Turbulent acceleration and reconnection

Two remaining widely discussed acceleration mechanisms are stochastic acceleration in magnetized turbulence (e.g. [Stawarz & Petrosian 2008](#), and references therein) and magnetic field line reconnection (e.g. [Sironi & Spitkovsky 2014](#); [Guo et al. 2015](#)). These possibilities are not mutually exclusive: the two processes would be expected to operate together in a turbulent magnetized plasma, and so we consider them together in this section. Magnetic reconnection is attractive in the context of Pic A because it naturally produces small-scale, localized acceleration regions, something which is not necessarily expected in the case of distributed turbulent acceleration, and these regions are associated with enhanced magnetic field strengths, increasing their observability in a synchrotron model; thus it is particularly suitable for explaining the small-scale flares in the jet. Reconnection can produce the flat electron energy spectrum that is observed out to the optical ([Gentry et al. 2015](#)) without difficulty ([Sironi & Spitkovsky 2014](#)) and the steeper X-ray spectrum could then be accounted for in the standard way by losses in a continuous-injection model (valid so long as the region over which we integrate observationally exceeds the loss spatial scale, as it does if the magnetic field strength is close to equipartition). Simulations such as those of [Sironi & Spitkovsky \(2014\)](#) show that the efficiency of reconnection as an acceleration mechanism depends on the jet magnetization parameter σ (and in particular requires $\sigma > 1$ in the emission regions), and so another attractive feature of the mechanism is that it can account for variations in the efficiency of production of X-rays, either within jets as in Pic A's inner and outer regions or between jets in different sources, by allowing σ to vary. Unfortunately, detailed numerical modelling of reconnection in the specific physical situation presented by Pic A's jet is intractable, because of the very large range of spatial scales involved (see discussion of the electron gyroradius in the previous subsection). Relativistic magnetohydrodynamic modelling (to give the field structure expected at the edge of the jet) together with some sub-grid model for the microphysics of reconnection might be able to make predictions about the frequency and intensity of flaring events that could be compared to our observations.

4.2 Hotspot spectrum, structure and variability

As we saw in Sections 3.3 and 3.4, the hotspot spectra are both reasonably well fitted with power-law spectra with $\Gamma \approx 1.9$, comparable to the best-fitting power law for the jet. The X-ray emission in both is much too bright to be inverse-Compton (specifically synchrotron self-Compton, the favoured mechanism for hotspots) with an equipartition field strength ([Hardcastle et al. 2004](#)). In the bright W hotspot, there is evidence for spectral steepening in the X-ray band, with the photon index being 1.9 at the soft end of the band and 2.2 at the high end (the break in photon index is 0.30 ± 0.05): this affects the compact bright component of the hotspot and may affect the more diffuse emission to its E as well. For an equiparti-

tion field strength of 16 nT (derived from fits to the data of [Meisenheimer et al. \(1997\)](#), using a spherical geometry, and thus indicative only) the synchrotron loss timescale of electrons radiating at an observed frequency corresponding to 7 keV is ~ 20 years, while the physical size of even the compact component of the hotspot is ~ 1 kpc, so losses of these electrons are inevitable. However, we know from the modelling of [Meisenheimer et al. \(1997\)](#) that there is a spectral break below the optical band, at around 10^{13} Hz, which should represent the point at which electron losses start to dominate over transport losses from the hotspot: electrons radiating at this frequency have a loss timescale of around 10^4 years, which is consistent with the observed physical size of the hotspot if we assume sub-relativistic outflow from the acceleration region. The further steepening of the spectrum in the X-ray band must then either represent the first signs of a high-energy cutoff in the acceleration spectrum, imposed by some property of the acceleration region, or evidence for additional loss processes for very high-energy electrons, either synchrotron, synchrotron self-Compton or adiabatic. It is not clear whether additional loss processes could produce as strong a change in the spectrum as is observed (a steepening in photon index over a factor 10 in photon energy, and so a factor of only 3 in electron energy) but a high-energy cutoff certainly could do so. Such a model would predict a steep spectrum in higher-energy observations, a result which can be tested with forthcoming *NuSTAR* observations.

The most unexpected result to emerge from our long-term monitoring is the apparent decrease in the W hotspot flux by ~ 10 per cent over the period between epochs 7 and 8, on a timescale of only a few months (Section 3.3). Taken at face value, this implies that a significant fraction of the X-ray emission must come from very small (sub-pc) regions of the hotspot. [Tingay et al. \(2008\)](#) have shown using high-resolution radio imaging that a small fraction of the radio flux in the hotspot (around 2 per cent) is produced by compact structures, with size scales of tens-hundreds of pc. If the variability we see is real, though, a larger fraction of the X-ray flux must come from structures that are even smaller in scale. Our observations provide some support to the model proposed by [Tingay et al. \(2008\)](#) in which much of the X-ray emission is produced in the compact components that they see in the radio, although we note the clear detection of extended X-ray emission as well, particularly from the 'bar' to the E of the main hotspot structure, which suggests that some of the X-ray emission is genuinely diffuse. However, the basic picture, in which compact regions play an important role in high-energy particle acceleration at the hotspot, clearly explains the observations of [Tingay et al.](#) and the variability we see, and also helps to explain the steepening of the X-ray spectrum at high energies. The most likely explanation for the compact regions seen in the radio is that they are due to localized magnetic field strength overdensities within the hotspot: such structures will be privileged sites for particle acceleration but will also necessarily be transient, since their excess of magnetic field strength will drive expansion (as pointed out by [Tingay et al.](#)). Variability in the X-ray and losses in the X-ray regime over and above those predicted from a simple one-zone model are both naturally expected in this picture. We might also expect some variability in the radio, and it would be interesting to investigate both the integrated variability of the hotspot and any variability in the small-scale radio features seen by [Tingay et al.](#)

The W hotspot, and quite possibly also the E hotspot if we accept the possible association between components R1 and X2, show offsets on kpc scales between the X-ray and radio peaks. These offsets have been seen in many other sources (see (e.g. [Hardcastle](#)

et al. 2002, 2007a; Perlman et al. 2010; Orienti et al. 2012)), and are always in the sense that the X-ray emission is further upstream (closer to the nucleus) than the radio. Georganopoulos & Kazanas (2003) proposed that some of the X-ray emission from hotspots might be produced by inverse-Compton upscattering by jet material of synchrotron photons from the shocked region: this predicts an offset in the sense (though not necessarily of the magnitude) that is observed. However, as noted by Hardcastle et al. (2007a), such a model fails to explain the offsets in sources aligned close to the plane of the sky, or in double hotspots. In Pic A, the lack of any spectral difference between the bright peak emission, where the offset is seen, and the more diffuse bar emission (Section 3.3) also argues against a role for inverse-Compton emission, which would be expected to have a flat spectrum. Morphologically, the bar region as seen in the X-ray has structure very similar to what is seen in the optical, where polarization clearly implies a synchrotron origin for the emission (e.g. Wagner et al. 2001; Saxton et al. 2002); both the optical and X-ray data, interpreted as synchrotron, require distributed, in situ particle acceleration in the W hotspot.

Finally, we draw attention to the very different structural properties of the E hotspot (Section 3.4), which contains mostly diffuse X-ray emission, extended over tens of kpc with only a few, faint (and possibly unrelated) compact components. Pic A is one of a number of well-studied broad-line FRIIs to show this difference between the jet-side and counterjet-side hotspots (see Hardcastle et al. (2007a) for the examples of 3C 227 and 3C 390.3). The natural explanation for this (and for various radio properties of large samples of hotspots, e.g. Bridle et al. 1994) is that there is some relativistic bulk motion downstream of the jet termination shock (Laing 1989; Komissarov & Falle 1996), an idea that has been discussed previously in the context of Pic A (HC05; Tingay et al. 2008), and that this suppresses on the counterjet side the bright compact emission associated with the jet termination itself, where the direction of the flow is still away from the observer, but enhances diffuse emission, which occurs in the backflow, directed towards the observer. Some consequences of this model were discussed by Bridle et al. (1994). Here we simply note that this is much easier to arrange (and likely to be much more significant for the observed properties of hotspots) if the mean bulk jet speed significantly exceeds the ‘beaming speed’ of $\sim 0.6c$, as in the models discussed in the previous subsection. In such a model the *hotspot* sidedness ratio (considering the compact component directly downstream from the termination shock) can be comparable to or even exceed the *jet* sidedness ratio, which arises from relatively slow-moving material in a boundary layer: this must be the case in Pic A if the terminations of the two jets are at all similar in the rest frame.

4.3 Magnetic field and electron distribution in the lobes

Pic A’s lobes, as the brightest clearly detected inverse-Compton lobes in the sky (Section 1.2), represent an excellent laboratory for studies of the nature of the lobe plasma. In Section 3.5 we measured a flux density for the lobes compatible with the earlier estimates of HC05 and a flat low-energy photon index of 1.57 ± 0.04 (statistical errors only), which is consistent with expectations for particle acceleration at strong shocks if the lobe emission is inverse-Compton from scattering of the CMB. Using simple one-zone lobe models and the code of Hardcastle et al. (1998), the flux we measure implies a mean magnetic field strength of around 0.4 nT in the lobes, a factor ~ 1.5 below the equipartition field strength. Pic A is very similar to other FRIIs in showing this slight departure from equipartition (Croston et al. 2005). The pressure from the radiating compo-

Table 6. Median and (10th, 90th) percentile radio/X-ray correlation slopes p for simulated lobes as a function of the field/electron correlation parameter s described in the text

s	Power-law slope p			
	Median	10th percentile	90th percentile	
0.00	0.169	0.009	0.232	
0.25	0.183	0.081	0.247	
0.50	0.229	0.136	0.272	
0.75	0.216	0.143	0.278	
1.00	0.233	0.153	0.334	
1.50	0.259	0.192	0.350	
2.00	0.308	0.191	0.402	

nents of the lobes (electrons and field) would then be around 10^{-13} Pa, which would provide pressure balance with an external thermal atmosphere only if the environment is very poor.

In Section 3.5 we drew attention to the very poor correlation between the X-ray and radio surface brightness in the lobes, which is clearly inconsistent with a model in which the variation in synchrotron surface brightness is caused by electron density variations in a constant magnetic field. Here we investigate⁸ the constraints placed by our observations on the family of models with the relationship between the local electron energy spectrum normalization and magnetic field described by a parameter s (Eilek 1989),

$$N_0 \propto \left(\frac{B}{B_0} \right)^s \quad (3)$$

Here $s = 0$ corresponds to the uniform electron density case discussed above, $s = 2$ corresponds to local equipartition, and we can conveniently denote the case with uniform field and arbitrarily varying electron density, which we have already ruled out, as $s = \infty$.

To do this we carry out a number of realizations of a spherical lobe with a Gaussian random magnetic field having a Kolmogorov power spectrum, using the code described by Hardcastle (2013) – we verified that this power spectrum for the field leads to a power spectrum in projected synchrotron emission that is consistent with what is observed in Pic A. The electron energy spectrum is assumed to be the same throughout, and, importantly, is chosen to reproduce the integrated spectrum of the lobes of Pic A (so that there is some spectral steepening in the radio with respect to the low-energy electrons that produce the inverse-Compton emission). This is necessary because the effect on emissivity of varying the magnetic field at a given observing frequency depends strongly on the local spectral index. The electron spectrum normalization is taken to depend everywhere on the local value of B as described by eq. 3. Synchrotron and inverse-Compton visualization were then carried out as described by Hardcastle (2013), the images were resampled to give the same number of independent data points as in the real images, and the slope of the power-law radio/X-ray surface brightness correlation was determined by binning in radio surface brightness and finding the errors via bootstrap in exactly the manner carried out for the real data in Section 3.5. This process was repeated for a number of different discrete values of s , and, for each s , repeated many times in order to form some kind of average over the randomly generated visualizations.

Results are given in Table 6, where we show both the median correlation slopes and the 10th and 90th percentile values to give

⁸ An earlier version of the modelling process described in this section was discussed by Goodger (2010), with similar conclusions.

some indication of the breadth of the distribution. We see, as expected, that higher values of s give rise to stronger correlations. The median correlation is always positive – simple geometrical effects guarantee that there will always be some positive correlation – but straight away we can see that only low values of s produce power-law slopes as flat as the one actually observed ($p = 0.047 \pm 0.038$). In fact, only $s = 0$ produces a slope as flat as the one observed in more than 10 per cent of the simulations (Table 6). This conclusion is robust to the introduction of uncorrelated noise into the electron densities, because this averages out both when integrating along a line of sight and when binning in radio surface brightness: for example, if we (unrealistically) add Gaussian noise with $\sigma = 0.5$ times the mean electron density to each volume element, truncating the electron density at zero when necessary, the results of Table 6 are essentially unaltered, although the scatter on a plot such as that of Fig. 11 is obviously increased. Even taking account of the errors on the fitted value of p , it is very hard to see how values of $s \geq 1$ can be reconciled with the data, and we suggest that this is additional strong evidence that the filamentary structures in lobes in general, and Pic A in particular, are dominated by variations in magnetic field strength with little correlated variation of the electron density. This conclusion is consistent with expectations from numerical modelling (Hardcastle & Krause 2014).

5 SUMMARY AND CONCLUSIONS

We have presented results from a long-term, sensitive programme of *Chandra* observations of the broad-line radio galaxy Pictor A, which give us unparalleled sensitivity to variability in compact components of the jet and hotspot coupled with by far the deepest view of inverse-Compton emission from a radio galaxy’s lobes. Key results may be summarized as follows:

(i) Both a jet and counterjet are detected extending all the way from the nucleus to the hotspot region (Section 3.2). The jet/counterjet flux ratio is completely incompatible with a beamed inverse-Compton origin for the X-rays, assuming the two jets are intrinsically identical: together with the now extremely well-constrained steep spectrum of the jet and with arguments from the detailed broad-band jet spectrum (Gentry et al. 2015) we conclude that the jets in Pic A are clearly synchrotron in origin (Section 4.1).

(ii) We have not seen any further flares at the level reported by M10, but there is further evidence for low-level, short-term variability in the jet (Section 3.2.4). At the same time, there is no evidence for any change in jet spectral index as a function of position, strongly arguing that the acceleration mechanism is constant along the jet, although acceleration *efficiency* may well vary (Section 3.2.2). We suggest that distributed, localized particle acceleration due to magnetic field reconnection may provide the best explanation for the observations (Section 4.1.4).

(iii) The well-studied bright W X-ray hotspot is shown to have a spectral steepening across the band, arguing for a spectral cutoff or at least significant losses in the high-energy electrons, and to be significantly offset with respect to the radio, as seen in a number of other hotspots. More importantly, we have found the first evidence for hotspot temporal variability on timescales of months to years (Section 3.3). These timescales correspond to spatial scales much smaller than the physical size of the hotspot, and we argue (Section 4.2) that this implies a significant contribution to the hotspot X-ray flux from one or a few very compact, bright regions, perhaps related to the compact radio sources seen by Tingay et al. (2008).

We suggest that these are transient features caused by very high localized magnetic field energy density, presumably a result of shock compression of the already complex magnetic field structure that is transported up the jet: if so, they would be expected to be variable at some level at all wavebands and it would be very interesting to monitor the hotspot flux evolution in the radio.

(iv) In the bright inverse-Compton lobes we show that there is a very poor correlation between radio and X-ray surface brightness (Section 3.5, which is consistent with models in which the electron density is relatively uniform and the variations in radio surface brightness are largely due to spatial magnetic field variations (Section 4.3).

What implications do these results have for other radio-loud AGN? As noted above (Section 1) Pic A’s X-ray jet is exceptional among jets identified as having a clear synchrotron origin in that it is detected for the whole of its length rather than as a few isolated ‘jet knots’. This, however, seems likely to be at least partly the result of modest Doppler boosting and of the proximity of Pic A rather than because it is physically unusual in some way. Another broad-line radio galaxy at a similar though slightly larger distance, 3C 111, shows a similar X-ray jet (Perlman et al. in preparation). The mechanisms that we have discussed for particle acceleration in the jet should be capable of operating in all FR II jets, though perhaps (particularly if our discussion of reconnection-related acceleration above is correct) with a wide range of intrinsic efficiencies. Therefore we would expect all FR II synchrotron jets to show similar behaviour: for example, we would expect steep (~ 2) photon indices in the X-ray with little variation along the jet. Unfortunately there are few sources with which to test this prediction, but, for example, it is consistent with observations of the knots of 3C 353 (Kataoka et al. 2008). A reconnection model offers a natural explanation for the tendency of X-ray jets to be brighter relative to the radio closer to the AGN, seen in Pic A, in 3C 353 and in many quasar jets (Marshall et al. 2001; Sambruna et al. 2004; Hardcastle 2006), if we assume that the boundary layer of the jet is initially more strongly magnetized and/or has more field reversals, and that these parameters are affected by dissipation along the jet. Models of this kind, with *in situ* acceleration of particles in many small regions with varying efficiency, do not have to produce a smooth broad-band synchrotron spectrum with a monotonically increasing spectral index as a function of frequency when integrated over regions much larger than the loss spatial scale (though they may do so, as we see in the jet of Cen A and in the individual knots in Pic A detected in the optical by Gentry et al. 2015). Consequently, synchrotron emission cannot be ruled out if, for example, a spectral flattening ($d\alpha/d\nu > 0$) is observed at some point.

It is important to emphasise, however, that nothing in our results rules out the alternative boosted inverse-Compton model for some or all of the X-ray emission in other beamed systems. In the picture we have outlined above, the X-ray emission will in fact always be a combination of the two processes. What we see will depend on both the intrinsic emissivity of the fast and slow components of the jets – which in the synchrotron case, we suggest, is dependent on local conditions in the boundary layer, and in the inverse-Compton case by the effectively unknown properties of the low-energy electrons in the fast spine of the jet – and on beaming, which will Doppler-suppress emission from the fast spine in all but the most closely aligned jets. High-resolution radio observations of large samples of FR II jets are required to test the model in which these systems have velocity structure and to investigate the properties of the fast-moving component if it exists. These may be pro-

vided by Jansky VLA and e-MERLIN observations in the coming years.

ACKNOWLEDGMENTS

We thank Rick Perley for providing radio images from Perley et al. (1997), Dan Schwartz and Dan Harris for helpful comments on an earlier draft of the paper, and the referee, Robert Laing, for numerous valuable comments on the content and presentation. This research has made use of data obtained from the *Chandra* Data Archive, and software provided by the *Chandra* X-ray Center (CXC) in the application packages CIAO and Sherpa. The Australia Telescope Compact Array is part of the Australia Telescope National Facility which is funded by the Commonwealth of Australia for operation as a National Facility managed by CSIRO. The National Radio Astronomy Observatory is a facility of the National Science Foundation operated under cooperative agreement by Associated Universities, Inc. This research made use of Astropy, a community-developed core Python package for astronomy (Astropy Collaboration et al. 2013) hosted at <http://www.astropy.org>, and of APLpy, an open-source plotting package for Python hosted at <http://aplpy.github.com>. The Centre for All-sky Astrophysics (CAASTRO) is an Australian Research Council Centre of Excellence, funded by grant CE110001020. MJH, JLG and JHC acknowledge support from the UK STFC via grants ST/M001008/1 and ST/M001326/1. Ł.S. was supported by Polish NSC grant DEC-2012/04/A/ST9/00083.

REFERENCES

- Astropy Collaboration et al., 2013, *A&A*, **558**, A33
- Barnacka A., Geller M. J., Dell’Antonio I. P., Benbow W., 2015, *ApJ*, **809**, 100
- Bennett C. L., et al., 2013, *ApJS*, **208**, 20
- Bicknell G. V., Begelman M. C., 1996, *ApJ*, **467**, 597
- Bridle A. H., Hough D. H., Lonsdale C. J., Burns J. O., Laing R. A., 1994, *AJ*, **108**, 766
- Cara M., et al., 2013, *ApJ*, **773**, 186
- Cash W., 1979, *ApJ*, **228**, 939
- Celotti A., Ghisellini G., Chiaberge M., 2001, *MNRAS*, **321**, L1
- Clausen-Brown E., Savolainen T., Pushkarev A. B., Kovalev Y. Y., Zensus J. A., 2013, *A&A*, **558**, A144
- Croston J. H., Hardcastle M. J., Birkinshaw M., 2005, *MNRAS*, **357**, 279
- Drake J. J., Ratzlaff P., Kashyap V., Edgar R., Izem R., Jerius D., Siemiginowska A., Vikhlinin A., 2006, in Society of Photo-Optical Instrumentation Engineers (SPIE) Conference Series. p. 1, doi:10.1117/12.672226
- Drake J., Ratzlaff P., Kashyap V., 2011, in Ness J.-U., Ehle M., eds, The X-ray Universe 2011. p. 61
- Eilek J. A., 1989, *AJ*, **98**, 244
- Eracleous M., Sambruna R., Mushotzky R. F., 2000, *ApJ*, **537**, 654
- Evans D. A., Kraft R. P., Worrall D. M., Hardcastle M. J., Jones C., Forman W. R., Murray S. S., 2004, *ApJ*, **612**, 786
- Fanaroff B. L., Riley J. M., 1974, *MNRAS*, **167**, 31P
- Gehrels N., 1986, *ApJ*, **303**, 336
- Gentry E. S., et al., 2015, *ApJ*, **808**, 92
- Georganopoulos M., Kazanas D., 2003, *ApJ*, **589**, L5
- Georganopoulos M., Perlman E. S., Kazanas D., McEnery J., 2006, *ApJ*, **653**, L5
- Goodger J., 2010, PhD thesis, University of Hertfordshire
- Goodger J. L., et al., 2010, *ApJ*, **708**, 675
- Grandi P., Guinazzi M., Maraschi L., Morganti R., Fusco-Femiano R., Fiocchi M., Ballo L., Tavecchio F., 2003, *ApJ*, **586**, 123
- Guo F., Liu Y.-H., Daughton W., Li H., 2015, *ApJ*, **806**, 167
- Hardcastle M. J., 2006, *MNRAS*, **366**, 1465
- Hardcastle M. J., 2013, *MNRAS*, **433**, 3364
- Hardcastle M. J., Croston J. H., 2005, *MNRAS*, **363**, 649
- Hardcastle M. J., Croston J. H., 2010, *MNRAS*, **404**, 2018
- Hardcastle M. J., Krause M. G. H., 2013, *MNRAS*, **430**, 174
- Hardcastle M. J., Krause M. G. H., 2014, *MNRAS*, **443**, 1482
- Hardcastle M. J., Alexander P., Pooley G. G., Riley J. M., 1998, *MNRAS*, **296**, 445
- Hardcastle M. J., Birkinshaw M., Cameron R., Harris D. E., Looney L. W., Worrall D. M., 2002, *ApJ*, **581**, 948
- Hardcastle M. J., Harris D. E., Worrall D. M., Birkinshaw M., 2004, *ApJ*, **612**, 729
- Hardcastle M. J., Croston J. H., Kraft R. P., 2007a, *ApJ*, **669**, 893
- Hardcastle M. J., et al., 2007b, *ApJ*, **670**, L81
- Harris D. E., Krawczynski H., 2006, *ARA&A*, **44**, 463
- Harris D. E., Biretta J. A., Junor W., Perlman E. S., Sparks W. B., Wilson A. S., 2003, *ApJ*, **586**, L41
- Harris D. E., Cheung C. C., Biretta J. A., Sparks W. B., Junor W., Perlman E. S., Wilson A. S., 2006, *ApJ*, **640**, 211
- Harris D. E., Cheung C. C., Stawarz Ł., Biretta J. A., Perlman E. S., 2009, *ApJ*, **699**, 305
- Intema H. T., van der Tol S., Cotton W. D., Cohen A. S., van Bemmel I. M., Röttgering H. J. A., 2009, *A&A*, **501**, 1185
- Jester S., Harris D. E., Marshall H. L., Meisenheimer K., 2006, *ApJ*, **648**, 900
- Jorstad S. G., et al., 2005, *AJ*, **130**, 1418
- Kataoka J., et al., 2008, *ApJ*, **685**, 839
- Komissarov S. S., Falle S. A. E. G., 1996, in Hardee P.E., Bridle A.H., Zensus J.A. ed., Energy Transport in Radio Galaxies and Quasars. ASP Conference Series vol. 100, San Francisco, p. 327
- Kraft R. P., Hardcastle M. J., Worrall D. M., Murray S. S., 2005, *ApJ*, **622**, 149
- Laing R. A., 1989, in Meisenheimer K., Röser H.-J. ed., Hotspots in Extragalactic Radio Sources. Springer-Verlag, Heidelberg, p. 27
- Laing R. A., Bridle A. H., 2002, *MNRAS*, **336**, 328
- Leahy J. P., Black A. R. S., Dennett-Thorpe J., Hardcastle M. J., Komissarov S., Perley R. A., Riley J. M., Scheuer P. A. G., 1997, *MNRAS*, **291**, 20
- Lee H., et al., 2011, *ApJ*, **731**, 126
- Marshall H. L., et al., 2001, *ApJ*, **549**, L167
- Marshall H. L., et al., 2010, *ApJ*, **714**, L213
- Meisenheimer K., Yates M. G., Röser H. J., 1997, *A&A*, **325**, 57
- Meyer E. T., Georganopoulos M., 2014, *ApJ*, **780**, L27
- Meyer E. T., Georganopoulos M., Sparks W. B., Godfrey L., Lovell J. E. J., Perlman E., 2015, *ApJ*, **805**, 154
- Migliori G., Grandi P., Palumbo G. G. C., Brunetti G., Stanghellini C., 2007, *ApJ*, **668**, 203
- Mingo B., Hardcastle M. J., Croston J. H., Evans D. A., Hota A., Kharb P., Kraft R. P., 2011, *ApJ*, **731**, 21
- Mingo B., Hardcastle M. J., Croston J. H., Dicken D., Evans D. A., Morganti R., Tadhunter C., 2014, *MNRAS*, **440**, 269
- Mullin L. M., Hardcastle M. J., 2009, *MNRAS*, **398**, 1989
- Nakamura M., Meier D. L., 2014, *ApJ*, **785**, 152
- Orienti M., Prieto M. A., Brunetti G., Mack K.-H., Massaro F., Harris D. E., 2012, *MNRAS*, **419**, 2338
- Perley R. A., Röser H. J., Meisenheimer K., 1997, *A&A*, **328**, 12
- Perlman E. S., Georganopoulos M., May E. M., Kazanas D., 2010, *ApJ*, **708**, 1
- Petrov L., Phillips C., Bertarini A., Murphy T., Sadler E. M., 2011, *MNRAS*, **414**, 2528
- Rees M. J., 1978, *MNRAS*, **184**, 61P
- Rieger F. M., Duffy P., 2004, *ApJ*, **617**, 155
- Robertson J. G., 1973, *Aust.J.Phys.*, **26**, 403
- Saito S., Stawarz Ł., Tanaka Y. T., Takahashi T., Sikora M., Moderski R., 2015, *ApJ*, **809**, 171
- Sambruna R. M., Eracleous M., Mushotzky R. F., 1999, *ApJ*, **526**, 60
- Sambruna R. M., Gambill J. K., Maraschi L., Tavecchio F., Cerutti R., Cheung C. C., Urry C. M., Chartas G., 2004, *ApJ*, **608**, 698

- Sault R. J., Teuben P. J., Wright M. C. H., 1995, in Shaw R.A., Payne H.E., Hayes J.J.E. ed., *Astronomical Data Analysis Software and Systems IV*. ASP Conference Series 77, San Francisco, p. 33
- Saxton C. J., Sutherland R. S., Bicknell G. V., Blanchet G. F., Wagner S. J., 2002, *A&A*, **393**, 765
- Schwartz D. A., et al., 2000, *ApJ*, **540**, L69
- Shepherd M. C., Pearson T. J., Taylor G. B., 1994, *Bulletin of the American Astronomical Society*, **26**, 987
- Sironi L., Spitkovsky A., 2014, *ApJ*, **783**, L21
- Stawarz L., Ostrowski M., 2002, *ApJ*, **578**, 763
- Stawarz L., Petrosian V., 2008, *ApJ*, **681**, 1825
- Stawarz L., Sikora M., Ostrowski M., Begelman M. C., 2004, *ApJ*, **608**, 95
- Swain M. R., Bridle A. H., Baum S. A., 1998, *ApJ*, **507**, L29
- Tavecchio F., Maraschi L., Sambruna R. M., Urry C. M., 2000, *ApJ*, **544**, L23
- Tavecchio F., Ghisellini G., Celotti A., 2003, *A&A*, **403**, 83
- Tingay S. J., et al., 2000, *AJ*, **119**, 1695
- Tingay S. J., Lenc E., Brunetti G., Bondi M., 2008, *AJ*, **136**, 2473
- Wagner S. J., Bicknell G., Szeifert T., 2001, in Laing R. A., Blundell K. M., eds, *Astronomical Society of the Pacific Conference Series Vol. 250, Particles and Fields in Radio Galaxies Conference*. p. 259
- Wardle J. F. C., Aaron S. E., 1997, *MNRAS*, **286**, 425
- Willott C. J., Rawlings S., Blundell K. M., Lacy M., 1999, *MNRAS*, **309**, 1017
- Wilson A. S., Young A. J., Shopbell P. L., 2001, *ApJ*, **547**, 740
- Wilson W. E., et al., 2011, *MNRAS*, **416**, 832
- Worrall D. M., 2009, *A&ARv*, **17**, 1
- Worrall D. M., Birkinshaw M., O'Sullivan E., Zezas A., Wolter A., Trinchieri G., Fabbiano G., 2010, *MNRAS*, **408**, 701
- Wykes S., Hardcastle M. J., Karakas A. I., Vink J. S., 2015, *MNRAS*, **447**, 1001
- Xu J., et al., 2014, *ApJ*, **794**, 97
- Zdziarski A. A., Sikora M., Pjanka P., Tchekhovskoy A., 2015, *MNRAS*, **451**, 5446